# Discovery and characterization of highly potent and selective allosteric USP7 inhibitors

# Discovery and Characterisation of Highly Potent & Selective Allosteric USP7 Inhibitors.

**Authors:** Gerald Gavory[1], Colin R O'Dowd[1], Matthew D Helm[1], Jakub Flasz[2], Elias Arkoudis[2], Anthony Dossang[1], Caroline Hughes[1], Eamon Cassidy[1], Keeva McClelland[1], Ewa Odrzywol[1], Natalie Page[1], Oliver Barker[1], Hugues Miel[1], Timothy Harrison[1,2*].

[1]Almac Discovery Ltd, Centre for Precision Therapeutics, 97 Lisburn Road, Belfast, Northern Ireland BT9 7AE, United Kingdom. [2]Centre for Cancer Research and Cell Biology, Queen's University, Belfast, Northern Ireland BT9 7AE, United Kingdom.

***Corresponding Author**: timothy.harrison@almacgroup.com

**ABSTRACT**

Given the importance of USP7 in oncogenic pathways, the identification of USP7 inhibitors has attracted considerable interest. Despite substantial efforts however, the development of validated deubiquitinase (DUB) inhibitors which exhibit drug-like properties and a well-defined mechanism of action has proved particularly challenging. In this article, we describe the identification, optimisation and detailed characterisation of highly potent ($IC_{50}$ < 10 nM) selective USP7 inhibitors together with their less active, enantiomeric counterparts. We also disclose for the first time co-crystal structures of a human DUB enzyme complexed with small molecule inhibitors which reveal a previously undisclosed allosteric binding site. Finally, we report the identification of cancer cell lines hyper-sensitive to USP7 inhibition ($EC_{50}$ < 30 nM) and demonstrate equal or superior activity in these cell models compared to clinically relevant MDM2 antagonists. Overall, these findings demonstrate the tractability and druggability of DUBs and provide important tools for additional target validation studies.

**Keywords:**

Ubiquitin

Deubiquitinase

Ubiquitin-Specific Protease

USP7

p53

Mdm2

## INTRODUCTION

Over the past three decades, protein ubiquitination has emerged as an important post-translational modification with roles in a plethora of cellular processes[1]. Dysregulation of the ubiquitin proteasome system (UPS) has been implicated in the pathogenesis of multiple human diseases including cancer, immune and inflammatory-related medical conditions[2,3]. Ubiquitin (Ub) is conjugated to protein substrates through the concerted action of E1, E2 and E3 enzymes and removed by deubiquitinating enzymes (DUBs)[4]. The approval and clinical success of the proteasome inhibitor Velcade® (bortezomib) and its successors has validated the UPS as a viable target for therapeutic intervention[5]. Manipulation of the UPS pathway upstream of the proteasome therefore presents new opportunities for the development of novel therapeutics with potentially enhanced specificity and reduced toxicity profiles[6].

The DUB family comprises 103 members sub-divided into 6 classes[7, 8]. USPs, which are cysteine proteases, represent the largest sub-family of DUBs with more than 50 family members reported[9]. USPs catalyse the removal of ubiquitin from target substrates thus preventing their induced-degradation by the proteasome and/or regulating their activation and subcellular localization, and as such represent an emerging and attractive target class[10-12]. Although the co-crystal structure of a viral DUB in complex with a non-covalent inhibitor has been reported[13], to date there have been no reports of a co-crystal structure of a human DUB in complex with a small molecule inhibitor.

Amongst all USPs, Ubiquitin Specific Protease 7 (USP7) has attracted the most attention due to its involvement in multiple oncogenic pathways[14]. Of particular importance, USP7 plays a key role in regulating the stability of MDM2, an oncoprotein and E3 ligase which promotes the proteosomal degradation of the tumor suppressor p53[15, 16, 17]. Beyond MDM2, USP7 has also been implicated in the regulation of several other proteins linked to cancer[14, 18-23], immunotherapy[24], glucose metabolism[25] and viral infections[26-28].

To date, several reports have described attempts to identify potent and selective USP7 inhibitors[29-36], however this has proved challenging with reported inhibitors generally exhibiting low (i.e. micromolar) potency, often coupled with sub-optimal physicochemical properties, poor stability and/or low selectivity[29, 35, 37]. In addition, redox properties of ligands can confound the interpretation of biological data[38]. Herein, we describe the discovery of highly potent (nM) and selective inhibitors of USP7. We demonstrate that lead compounds inhibit USP7 in a non-covalent and reversible manner, and confirm direct binding to the target by orthogonal methods including the first reported high resolution co-crystal structures of USP7 in complex with small molecule inhibitors. These inhibitors possess excellent *in vitro* selectivity for USP7 and potently engage endogenous USP7 at concentrations which are similar to their biochemical potencies. The observed target engagement translates into degradation of MDM2, stabilisation of p53 and induction of p21 in multiple cell lines. Finally, cell lines which are hyper-sensitive to USP7 inhibition have been identified, thus providing new insights and directions for the potential development of USP7 inhibitors.

## RESULTS

### Identification of small-molecule USP7 inhibitors

Due to the difficulties in identifying high quality hit matter for DUBs using HTS[39], we decided to utilize fragment-based methods for the identification of USP7 inhibitors[40]. We used Surface Plasmon Resonance (SPR) for primary hit finding and screened 1946 fragments against the catalytic domain of USP7, followed by the synthesis, purchase and testing of additional fragments. From this work, Fragments **A** and **B** were identified as USP7 binders (Table 1). To complement our fragment-based approaches, we also synthesised and profiled examples of all disclosed USP7 inhibitors[29, 41], and by combining features of these published molecules with USP7 binding fragments (e.g. Fragment **B**, *manuscript in preparation*) we were ultimately able to generate novel compounds with reasonable affinity for USP7 as exemplified by **1** ($IC_{50}$ = 13.1 μM, **Table 1** and **Supplementary Figure 1a**). Compound **1** is chemically stable, has high aqueous solubility (>200 μM at $pH_{7.4}$) and is devoid of redox liabilities which may lead to the non-selective and spurious inhibition of USP7 (**Table 1**)[42]. We also confirmed inhibition of USP7 in a second assay format ($IC_{50}$ = 15.1 μM, **Table 1**) using a non-isopeptide linked substrate (Ub-Rh110). In addition, the binding of **1** to USP7 was confirmed by an orthogonal biophysical technique (SPR, $K_d$ = 7.7 μM, **Supplementary Figure 1b** and **Table 1**). Our SPR data also indicated **1** was a reversible binder ($k_{off}$ = 0.25 $s^{-1}$) which was further confirmed using a high-dilution biochemical assay (**Supplementary Figure 1c**). Collectively, these data confirm **1** as a genuine, reversible inhibitor of USP7 and a potentially tractable starting point suitable for further optimization.

**Co-crystal structure of USP7 bound with an inhibitor**

A key breakthrough in the development of potent and selective USP7 inhibitors was the finding that the introduction of a chiral methyl group ((*R*) stereochemistry) at the benzylic position of the phenethylamide chain increased USP7 inhibitory activity by up to 40-fold. Thus, **2** ($IC_{50}$ = 0.3 μM, **Table 1**) represented the first sub-μM USP7 inhibitor from this series. Importantly in the context of identifying negative control compounds, we observed a significant difference in activity between **2** and its enantiomer ***ent*-2** ($IC_{50}$ = 46.0 μM, **Table 1**).

The X-ray crystal structure of **2** in complex with USP7 was subsequently solved at high-resolution (2.2 Å, **Figure 1a**). The protein was observed to be in a conformation similar to the USP7 *apo* structure (PDB: 1NB8), with a disrupted catalytic triad and an overall Cα RMSD of 1.03 Å (see **Supplementary Figure 2**). The crystal structure also revealed key conformational changes that enable ligand binding: Phe409 adopts a novel side chain conformation not seen in either the *apo* or ubiquitin-conjugated USP7 structures available in the PDB (1NB8 and 1NBF respectively). This side chain movement creates a hydrophobic cavity occupied by the phenyl ring of **2** (**Figure 1b**). The loop between Gly458 and Gly463 also changes conformation (see **Supplementary Figure 3)**, positioning His461 between the ligand and the catalytic cysteine. The ligand therefore sits in an exo-site *ca*. 5.5 Å away from the catalytic cysteine Cys223 (as measured from the carbonyl group) and partially protrudes into the channel normally occupied by the C-terminal tail of ubiquitin (**Figure 1c**). The folded conformation of the ligand is reinforced by allylic 1,3-strain between the CH

of the chiral centre and the phenyl ring. Our analysis also indicates that **2** adopts a folded conformation in which the phenyl ring is packed against the piperidine ring, creating a potential CH-π intra-molecular interaction between a piperidine *C*-3 axial hydrogen and the aromatic group (**Figure 1b**). The co-crystal structure also provided a potential explanation at the molecular level for the difference in activity between **2** and its enantiomer (***ent*-2**). Inversion of the ligand stereo centre in the structure leads to a direct steric clash with His461 (**Supplementary Figure 4**). Together, this study reveals the first reported co-crystal structure of a DUB enzyme bound to a small molecule inhibitor in a novel site situated 5.5 Å from the catalytic cysteine (see **Supplementary Figures 5a-d** for further details)

**Optimisation of 2 provides highly potent USP7 inhibitors**

Using the co-crystal structure to facilitate structure-based design, we were able to further optimise the potency of compound **2** by modifying the core heterocycle and building off the heterocyclic ring into the pocket containing Gln351. This led to **3** ($IC_{50}$ = 6.0 nM; **Table 1**) and provided a further *ca*. 50-fold increase in potency relative to **2**. In order to confirm the determinants of binding, we solved the high-resolution (1.7 Å) crystal structure of a close analogue of **3** (compound **4**, $IC_{50}$ = 22.0 nM, **Figure 2a**) in complex with USP7. This co-crystal structure shows a high degree of similarity to the previously described complex of USP7 with **2** (**Figure 1a**). The Cα RMSD is 0.35 Å and the same side chain movements which create the hydrophobic pocket and the same pattern of hydrogen bonds are observed in both structures. The structure reveals how the benzylic amine extension to the heterocyclic core allows the amine

to form additional hydrogen bonds with Gln351 and two adjacent bridging waters while *N*-1 of the pyrazole can form a hydrogen bond with Phe409 instead of the pyrimidone carbonyl, leading to a significant increase in overall potency (**Figure 2a**). The catalytic triad is also misaligned. An overlay of the co-crystal structures of **2** and **4** in complex with USP7 is shown in **Figure 2b** (See also **Supplementary Figures 6a-c** for further details).

**Biochemical and biophysical profiling of 3 and *ent*-3.**

The detailed biochemical and biophysical profiling of **3** is compiled in **Table 1**. **3** is free of redox liabilities, is highly soluble and is 400-fold more active than its enantiomer ***ent*-3** ($IC_{50}$ = 2.4 µM; **Supplementary Figure 7a**, **Table 1**). **3** was also confirmed to be highly potent in an alternative assay format using the Ub-Rh110 substrate ($IC_{50}$ = 1.5 nM; **Table 1**). Characterisation by SPR revealed tight binding of **3** to USP7 ($K_d$ = 2.0 nM; **Supplementary Figure 7b**; **Table 1**). Under similar conditions, ***ent*-3** was confirmed to be a much weaker binder ($K_d$ = 5.0 µM). Subsequent kinetic analysis by SPR demonstrated that the potency gain obtained during compound optimisation was driven by an increase in target site occupancy as evidenced by the slower $k_{off}$ value for **3** ($k_{off}$ = 0.0004 $s^{-1}$; $t_{1/2}$ = 28.4 min) relative to **1** ($k_{off}$ = 0.25 $s^{-1}$; $t_{1/2}$ = 2.7 s).

**Determination of a non-competitive mode of inhibition**

Kinetic experiments were subsequently performed to characterise the mode of inhibition of USP7 by these inhibitors using the most potent compound **3** as a representative example (**Supplementary Figures 8a, b**). Lineweaver-Burk analysis

revealed that **3** acts as a non-competitive inhibitor. The apparent $K_m$ value for Ub-AMC was calculated as 1.9 µM and the inhibitory constant for **3** derived from this analysis ($K_i$ = 5.5 nM) was in excellent agreement with the $IC_{50}$ value obtained previously ($IC_{50}$ = 6.0 nM; **Table 1**). An Eadie-Hofstee analysis of the initial Michaelis-Menten dataset was performed, which confirmed the non-competitive mode of inhibition (**Supplementary Figure 8c**). In a separate experiment, USP7 was assayed with increasing concentration of the Ub-AMC substrate. Under the conditions of this experiment, the $IC_{50}$ values for **3** were independent of the substrate concentration further supporting the non-competitive mode of inhibition (average $IC_{50}$ = 1.0 nM, see **Supplementary Figure 9**).

**3 is highly selective against DUBs, proteases and kinases**

One long standing question in DUB research has related to the degree of selectivity achievable when targeting this enzyme class[43]. To address this question, we next assessed the selectivity profile of our inhibitors against a panel of DUBs (n=39; DUBprofiler™). In these experiments, **3** was screened at a fixed concentration of 100 µM and showed no significant activity (<20% inhibition) against 21 USPs and 17 other DUBs across the various sub-family members (**Figure 3**). We extended our screening to alternative target classes which indicated no significant off-targeting effect at 10 µM against a panel of 63 proteases or 49 representative kinases (**Supplementary Figures 10a and b**). Together these data demonstrate that high selectivity for inhibition of USP7 can be achieved *versus* DUBs and other target classes (>1000-fold).

**3 Demonstrates highly potent target engagement in cells**

We then investigated whether **3** was capable of interacting with endogenous USP7. Cells were treated with increasing concentration of inhibitor, lysed and the ubiquitin-propargylamine (Ub-PA) probe was then added. **3** efficiently competed with the Ub-PA probe in a concentration-dependent manner ($EC_{50}$ = 49 nM, **Figure 4a**). Only a minimal (<10-fold) cellular drop-off in the activity of **3** was observed relative to the biochemical activity ($IC_{50}$ = 6.0 nM) consistent with the non-competitive mode of inhibition demonstrated previously. ***Ent*-3** had no significant effect on target engagement ($EC_{50}$ > 50 μM; **Figure 4a**). Using a similar protocol, we assessed the selectivity of **3** in cells and demonstrated lack of target engagement against USP47 ($EC_{50}$ > 50 μM; **Figure 4b**), the closest homologue of USP7. Off-target activity against USP47 has been previously reported for USP7 inhibitors[31, 34]. A homology model of USP47 was created based on our USP7 co-crystal structures (**Supplementary Figure 11a**). Sequence alignment indicated that 6 residues within 5.0 Å of the compound binding site are different in USP47 relative to USP7 (**Supplementary Figure 11b**) providing a molecular basis for this selectivity. We extended our cellular investigations beyond USP47 to other USPs and again showed no effect on target engagement at concentrations up to 50 μM (**Figure 4b**). This data is consistent with the lack of measurable biochemical inhibition against these USPs ($IC_{50}$ > 100 μM; **Figure 3**). Together, these studies demonstrate good cellular permeability, potent target engagement with endogenous USP7 and excellent selectivity in cells against selected DUBs including USP47.

**3 increases p53 and decreases MDM2 total levels in cells**

We next evaluated the effect of **3** on downstream pathway components of USP7 signalling. HCT116 cells were treated with increasing concentrations of **3** for 2 h and lysed for western blotting analysis probing for key components of the USP7/MDM2 axis. Whilst the total USP7 protein levels remained steady, levels of p53 increased in a concentration-dependent manner (**Figure 5a**). The levels of p21 protein mirrored this increase in p53 indicating that the transcriptional activity of p53 was also restored. Importantly, these effects on p53 and p21 were independent of a genomic stress response as evidenced by the absence of p53 phosphorylation on Serine 15. Concomitantly, the levels of the MDM2 oncoprotein decreased in a concentration dependent manner. As shown in **Figure 5b**, these observations were also extended to the MCF7 cell line. In both cases, reduced levels of MDM2 could be rescued by the addition of the proteasome inhibitor MG132. The reduced levels of MDM2 following treatment with **3** contrasted markedly with the significant increase in MDM2 total protein levels induced by SAR405838 (**Figures 5a-b**); a characteristic of MDM2 antagonists caused by the feedback loop between p53 and MDM2[44, 45]. By comparison, ***ent*-3** had no significant effect on the total levels of p53, p21 or MDM2 (**Figures 5a-b**).

We next performed a quantitative analysis of ubiquitinated MDM2 levels using the commercial MDM2 whole cell lysate kit from MSD in the MDM2 amplified osteosarcoma cell line SJSA-1. Our data confirmed a potent effect of **3** on the total levels of ubiquitinated MDM2 ($EC_{50}$ = 55.0 nM, **Figure 5c, Table 1**) with a significantly reduced activity for ***ent*-3** ($EC_{50}$ > 20 μM). Altogether, these observations are consistent with the expected mechanism of action of a USP7 inhibitor, in which a

decrease in the levels of the oncogene MDM2 restores both the levels and transcriptional activity of the tumor suppressor p53[15, 46].

**Identification of cell lines hyper-sensitive to 3**

Having demonstrated target engagement and pathway modulation, we next assessed the anti-proliferative effects of **3**. To this end, we profiled **3** in a panel of cancer cell lines and identified a subset of lines hyper-sensitive to USP7 inhibition including the acute lymphoblastic leukemia cell line RS4;11. Follow-up studies using a viability assay performed at 72 h confirmed acute sensitivity to **3** ($EC_{50}$ = 2.0 nM, **Supplementary Table 3** and **Supplementary Figure 12a**). A time-course analysis by western blotting (8 to 72 h post treatment) revealed a strong and sustained effect on the total levels of p53 which was mirrored by the induction of p21 (**Supplementary Figure 12b**). We also observed a strong, time-dependent apoptotic response in this cell line as evidenced by both PARP and caspase 3 cleavage. Interestingly, the apoptotic response was time-shifted compared to treatment with the MDM2 antagonist SAR405838. Under identical experimental conditions, ***ent*-3** had no effect on p53 and p21 levels or apoptosis over this time-course and only had a weak impact on cell growth ($EC_{50}$ = 2.2 µM). The acute sensitivity of RS4;11 cells to **3** is in line with the potent target engagement we observed in this cell line ($EC_{50}$ = 6.0 nM, **Supplementary Figure 12c**).

Hyper-sensitivity to **3** could be extended to solid tumor cell lines including prostate (LNCaP, $EC_{50}$ = 29.0 nM, **Supplementary Figure 13a**; **Supplementary Table 3**). In this cell line, we again observed potent target engagement ($EC_{50}$ = 7.0 nM) with excellent

selectivity in cells over 4 other USP's including USP47 (**Supplementary Figures 13c** and **d**), which translated into a significant increase in ubiquitination of MDM2 protein following treatment with **3** (but not ***ent-3***, **Supplementary Figure 13e**). As described previously for the RS4;11 cell line, no significant effect on cell growth was observed following treatment with ***ent*-3** ($EC_{50}$ = 9.3 μM). Intriguingly, we observed that the modulation of p53 and p21 was less marked in this cell line than in RS4;11 cells and that the effect was typically observed at an earlier time point (8 h for p53 and up to 48 h for p21; **Supplementary Figure 13b**). In addition, we could not detect any significant degree of apoptosis in this cell line (as judged by the lack of caspase 3 and PARP cleavage) following treatment with **3** up to 72 h. Similar observations have been made following treatment with the MDM2 antagonist SAR405838 (**Supplementary Figure 13b**). This data is consistent with previously published studies using MDM2 antagonists in the LNCaP cell line where caspase-3 independent cell death has been described[45]. Further studies will be required to elucidate the mechanism(s) of cell death in this cell line.

**Benchmarking the activity of 3 against MDM2 antagonists**

To further investigate the potential therapeutic relevance of USP7 inhibitors, we next performed benchmarking experiments *versus* several MDM2 antagonists. Included in these studies were nutlin-3a, RG7112 and SAR405838. Both the RS4;11 and LNCaP cell lines have been previously shown to be highly responsive to MDM2 antagonists[44, 45]. Under identical experimental conditions, **3** compared very favourably to all three MDM2 antagonists (**Supplementary Figures 14a-b**). For example, **3** was found to be 70-fold more potent than nutlin-3a, 30-fold more potent

than RG7112 and 16-fold more potent than SAR405838 in the RS4;11 cell line (**Supplementary Table 3**). A similar ranking was observed in the LNCaP cell line. It will be important in future studies to further understand and delineate both the commonalities and differences between USP7 inhibitors and MDM2 antagonists. For instance, we have already observed that the osteosarcoma cell line SJSA-1 is sensitive to MDM2 antagonists ($EC_{50}$ = 100.0 nM and 320.0 nM for SAR405838 and RG7112 respectively) but resistant to treatment with **3** ($EC_{50}$ > 20 µM, **Supplementary Figure 14c** and **Supplementary Table 3**). Interestingly, under identical experimental conditions to those in which we observed full target engagement in the RS4;11 and LNCaP cell lines, only partial target engagement was observed in the SJSA-1 cell line even at high USP7 inhibitor concentrations (**Supplementary Figure 14d**). The above observations are encouraging and further mechanistic studies aimed at fully understanding the dependence on the p53 gene status and at precisely defining the scope of application of these USP7 inhibitors are warranted and will be reported at a later stage.

**Discussion**

DUBs have emerged as an attractive target class for the development of first in class medicines with potential for high therapeutic impact. However, despite 15 years of intense research, DUBs have proved largely refractory to drug discovery efforts. The development of genuine DUB inhibitors combining drug-like properties with a well-defined mode of inhibition thus remains a high priority for the research community.

USP7 has attracted special attention due to its established connections to known oncogenic pathways and other disorders[14]. The prospect of simultaneously restoring the cellular levels and function of p53 whilst promoting the degradation of the oncogenic E3 ligase MDM2 is particularly appealing. USP7 inhibitors have been described previously in literature publications, however many of these scaffolds have typically lacked high potency, stability, selectivity and/or a well-defined mechanism of action[29, 36, 37]. To the best of our knowledge the data reported herein represents the first published examples of highly potent (nM), selective and reversible small molecule DUB inhibitors with a clearly defined mode of binding to USP7 underpinned by high-resolution X-Ray structural information.

We prosecuted hit-finding using a combination of fragment-based screening and rational design. Using our UbiPlex™ assay platform, the early chemical hit matter identified (e.g. **1**) was optimized leading to the identification of **2** and **3** (**Table 1**). We demonstrated that these inhibitors are highly soluble, chemically stable and free of redox recycling activity (**Table 1**), which can otherwise lead to the non-specific and/or spurious inhibition of DUBs. Biochemical activity was demonstrated in two different assay formats and binding was orthogonally validated using SPR (**Supplementary Figures 1a-b**, **7a-b**; **Table 1**). Finally, X-ray structural studies provided unambiguous binding validation of this series of inhibitors to USP7. Analysis of these high-resolution (1.7-2.3 Å) structures revealed that the inhibitors bind outside of the active site in a previously undisclosed allosteric pocket situated 5.5 Å from the catalytic cysteine. Our analysis also revealed a binding mode with a folded conformation of the ligand, stabilised by an intra-molecular CH-π interaction

between a piperidine CH and the phenyl group of the phenylbutanamide side-chain (**Figures 1b**; **2a-b**). The ligand-bound structures are reminiscent of the *apo* structure of USP7 in which the catalytic triad remains misaligned and in a non-functional, catalytically incompetent state (**Supplementary Figure 2**). We postulate that a potential mechanism of action of these molecules may be to prevent the alignment of the catalytic triad within the active site of USP7 and by partially protruding into the channel which normally accommodates the C-terminus of ubiquitin, the ligands may additionally induce a local distortion of the Ub tail, thus precluding catalysis. These two mechanisms are not necessarily mutually exclusive and could act in concert. Furthermore, both models are consistent with the non-competitive mode of inhibition demonstrated during the course of our studies (**Supplementary Figure 8**).

Structure-based design was used to further optimise our early leads culminating in the identification of our most potent inhibitor **3** which consistently exhibited $IC_{50}$ values in the single digit nM range (**Table 1**). High selectivity (>10,000-fold) against other members of the USP and DUB families was demonstrated (**Figure 3**). The high specificity of **3** for USP7 was confirmed in cells as evidenced by the lack of target engagement against USP47 (up to 50 µM), the closest USP7 homologue (**Figure 4b**) [31, 34]. Under similar conditions, **3** proved to be highly potent against USP7 in this cellular target engagement assay ($EC_{50}$ = 49.0 nM, **Figure 4a**). We extended our off-target screening to alternative target classes which indicated no significant off-targeting effect at 10 µM against a panel of 63 proteases and 49 kinases (**Supplementary Figures 10a, b** respectively).

In order to explore how potentially relevant the structural information may be in designing inhibitors for other USPs, we performed a comparison of the key residues forming the exosite for Compounds **2** and **4** with the equivalent residues from the published crystal structures of other USP's (**Supplementary Figure 15**). Interestingly, the key residues involved in binding are conserved in each of the USP's. However, we observe significant alterations in certain sidechain conformations for some residues and target specific features which may preclude binding of molecules such as **2** and **4**, consistent with their excellent selectivity profiles. However the relatively high degree of conservation in the residues forming the binding site suggests that there may be an opportunity to utilise these ligands for the design of inhibitors of other USPs, and this remains an area of ongoing investigation.

With potent, selective chemical probes in hand, concentration dependent pathway modulation was subsequently demonstrated leading to increased protein levels of p53 and reduced levels of the oncoprotein MDM2. In addition, we observed a concomitant induction in p21 protein levels (**Figures 5a-b**). The absence of p53 phosphorylation on Ser15 following treatment with **3** together with the absence of any effect on protein levels (of p53, MDM2 or p21) following treatment with ***ent*-3** demonstrates the non-genotoxic, on-target nature of these effects. These observations were extended to multiple cell lines (**Supplementary Figures 12b** and **13b**) and taken together are consistent with the expected mechanism of action of a USP7 inhibitor. Next, we assessed the anti-proliferative effects of these compounds and in so doing identified cell lines hyper-sensitive ($EC_{50}$ < 30 nM) to USP7 inhibition

which included both haematological (RS4;11) and solid tumor cell lines (LNCaP) (**Supplementary Figures 12a** and **13a**). A robust time- and concentration-dependent apoptotic induction was observed in RS4;11 cells as evidenced by PARP and caspase 3 cleavage. Consistent with previously published studies, no marked apoptotic response was detected in the LNCaP cell line using either USP7 inhibitor **3** or the highly potent MDM2 antagonist SAR405838. ***Ent*-3** had no marked effect on apoptosis and exerted no significant anti-proliferative effect in either of these two cell lines (**Table 2**, **Supplementary Figures 12a-b, 13a-b**). The marked differences in behaviours between **3** and ***ent*-3** reflects the value and utility of enantiomeric pairs as chemical probes to confirm on-target effects during target validation studies.

Finally, we benchmarked the anti-proliferative activity of **3** against established MDM2 antagonists. Profiled head-to-head, **3** was more potent than all three MDM2 antagonists in the RS4;11 and LNCaP cell lines (**Supplementary Figures 14a-b**). Taken together, these benchmarking studies represent an important proof-of-concept for USP7 inhibitors and justify further cellular and *in vivo* profiling. Carefully-designed *in vivo* efficacy and toxicity studies will then be required to fully define the therapeutic relevance, potential therapeutic index and scope of pharmacologically targeting USP7. Emphasis will be placed in future studies on assessing the p53-dependence and unveiling the markers of sensitivity to USP7 inhibitors as well as in delineating the overlap and differences in activity when compared to MDM2 antagonists. In this regard, potential differences have already been observed as evidenced by the lack of

response of the SJSA-1 cell line to **3** compared to the high sensitivity to SAR405838 and RG7112 (**Supplementary Figure 14c**, **Supplementary Table 3**).

In conclusion, we report herein the first highly potent (nM), reversible and selective inhibitors of USP7 which exhibit a well-characterised binding mode and modulate the total levels of downstream targets of USP7 including MDM2, p53 and p21. As part of these studies, we have demonstrated the ligandability and tractability of USP7 as a target and reported the first co-crystal structures of a DUB with high affinity small molecule inhibitors. We have additionally identified cell lines hyper-sensitive to USP7 inhibitors and demonstrated potency in cells comparable or superior to that of clinically relevant MDM2 antagonists. These findings represent important milestones in terms of feasibility and proof-of-concept studies, and we anticipate that these enantiomeric chemical probes will be of direct relevance and utility to the USP7 research community and more broadly to all those aiming to identify and develop innovative DUB therapeutics.

**ACKNOWLEDGEMENTS**

The authors thank collaborators at Ubiquigent (Dundee, UK), Boston Biochem (Boston, US) and Beactica (Uppsala, Sweden) for their contributions, as well as Crelux GmbH (Martinsried, Germany) for solving the crystal structures, and Prof. C. Scott and Dr James Burrows (Queen's University, Belfast) for helpful discussions and for providing the HA-Ub plasmid respectively. This study was supported by the Almac Group, the European Regional Development Fund and Invest Northern Ireland (Grant RD1010668).

## Author Contributions

TH conceived the concept and directed the research. CROD and GG helped conceive and develop the concept and designed and supervised medicinal chemistry and biology experiments. MDH, EA, JF and HM carried out the design, synthesis and characterization of compounds. AD performed SPR experiments. CH, KMcC, EO , EC, AD and NP carried out compound screening, target validation and biochemical and cellular profiling studies. OB carried out computational modelling and structural analysis. TH and GG wrote the manuscript with input from other authors.

## Competing Financial Interests Statement

The authors declare no competing financial interest.

**References**


1. Yau, R. & Rape, M. The increasing complexity of the ubiquitin code. *Nat Cell Biol* **18**, 579-586 (2016).
2. Huang, X. & Dixit, V.M. Drugging the undruggables: exploring the ubiquitin system for drug development. *Cell Res*, 1-15 (2016).
3. Zheng, Q. *et al.* Dysregulation of Ubiquitin-Proteasome System in Neurodegenerative Diseases. *Front Aging Neurosci* **8:303**, 1-8 (2016).
4. Zhang, W. & Sidhu, S.S. Development of inhibitors in the ubiquitination cascade. *FEBS Lett* **588**, 356-367 (2014).
5. Merin, N.M. & Kelly, K.R. Clinical use of proteasome inhibitors in the treatment of multiple myeloma. *Pharmaceuticals (Basel)* **8**, 1-20 (2014).
6. Sheridan, C. Drug Makers Target UPS Anew *Nat Biotech.* **33**, 1115-1117 (2015).
7. Abdul Rehman, S.A. *et al.* MINDY-1 Is a Member of an Evolutionarily Conserved and Structurally Distinct New Family of Deubiquitinating Enzymes. *Mol Cell* **63**, 146-155 (2016).
8. Clague, M.J. *et al.* Deubiquitylases from genes to organism. *Physiol Rev* **93**, 1289-1315 (2013).
9. Ye, Y., Scheel, H., Hofmann, K. & Komander, D. Dissection of USP catalytic domains reveals five common insertion points. *Mol Biosyst* **5**, 1797-1808 (2009).
10. Pal, A., Young, M.A. & Donato, N.J. Emerging potential of therapeutic targeting of ubiquitin-specific proteases in the treatment of cancer. *Cancer Res* **74**, 4955-4966 (2014).
11. Heideker, J. & Wertz, I.E. DUBs, the regulation of cell identity and disease. *Biochem J* **465**, 1-26 (2015).
12. D'Arcy, P., Wang, X. & Linder, S. Deubiquitinase inhibition as a cancer therapeutic strategy. *Pharmacol Ther* **147**, 32-54 (2015).
13. Ratia, K. *et al.* A noncovalent class of papain-like protease/deubiquitinase inhibitors blocks SARS virus replication. *Proc Natl Acad Sci U S A* **105**, 16119-16124 (2008).
14. Nicholson, B. & Suresh Kumar, K.G. The multifaceted roles of USP7: new therapeutic opportunities. *Cell Biochem Biophys* **60**, 61-68 (2011).
15. Cummins, J.M. *et al.* Tumour suppression: disruption of HAUSP gene stabilizes p53. *Nature* **428**, doi:10.1038/nature02501 (2004).
16. Kon, N. *et al.* Inactivation of HAUSP in vivo modulates p53 function. *Oncogene* **29**, 1270-1279 (2010).
17. Tavana, O. & Gu, W. Modulation of the p53/MDM2 interplay by HAUSP inhibitors. *J Mol Cell Biol*, 1-8 (2016).
18. Song, M.S. *et al.* The deubiquitinylation and localization of PTEN are regulated by a HAUSP-PML network. *Nature* **455**, 813-817 (2008).
19. Wu, H.T. *et al.* K63-polyubiquitinated HAUSP deubiquitinates HIF-1alpha and dictates H3K56 acetylation promoting hypoxia-induced tumour progression. *Nat Commun* **7**, 13644 (2016).
20. Tavana, O. *et al.* HAUSP deubiquitinates and stabilizes N-Myc in neuroblastoma. *Nat Med* **22**, 1180-1186 (2016).

21. Wang, Q. *et al.* Stabilization of histone demethylase PHF8 by USP7 promotes breast carcinogenesis. *J Clin Invest* **126**, 2205-2220 (2016).
22. Zhou, Z. *et al.* Deubiquitination of Ci/Gli by Usp7/HAUSP Regulates Hedgehog Signaling. *Dev Cell* **34**, 58-72 (2015).
23. van der Horst, A. *et al.* FOXO4 transcriptional activity is regulated by monoubiquitination and USP7/HAUSP. *Nat Cell Biol* **8**, 1064-1073 (2006).
24. van Loosdregt, J. *et al.* Stabilization of the transcription factor Foxp3 by the deubiquitinase USP7 increases Treg-cell-suppressive capacity. *Immunity* **39**, 259-271 (2013).
25. Hall, J.A., Tabata, M., Rodgers, J.T. & Puigserver, P. USP7 attenuates hepatic gluconeogenesis through modulation of FoxO1 gene promoter occupancy. *Mol Endocrinol* **28**, 912-924 (2014).
26. Jager, W. *et al.* The ubiquitin-specific protease USP7 modulates the replication of Kaposi's sarcoma-associated herpesvirus latent episomal DNA. *J Virol* **86**, 6745-6757 (2012).
27. Meredith, M., Orr, A, Everett, R Herpes simplex virus type 1 immediate-early protein Vmw110 binds strongly and specifically to a 135-kDa cellular protein. *Virology* **200**, 457-469 (1994).
28. Holowaty, M.N.e.a. Protein Profiling with Epstein-Barr Nuclear Antigen-1 Reveals an Interaction with the Herpesvirus-associated Ubiquitin-specific Protease HAUSP/USP7. *J Biol Chem* **278**, 29987-29994 (2003).
29. Kemp, M. Recent Advances in the Discovery of Deubiquitinating Enzyme Inhibitors. *Prog Med Chem* **55**, 149-192 (2016).
30. Chen, C. *et al.* Synthesis and biological evaluation of thiazole derivatives as novel USP7 inhibitors. *Bioorg Med Chem Lett* **27**, 845-849 (2017).
31. Weinstock, J. *et al.* Selective Dual Inhibitors of the Cancer-Related Deubiquitylating Proteases USP7 and USP47. *ACS Med Chem Lett* **3**, 789-792 (2012).
32. Reverdy, C. *et al.* Discovery of specific inhibitors of human USP7/HAUSP deubiquitinating enzyme. *Chem Biol* **19**, 467-477 (2012).
33. Colland, F. *et al.* Small-molecule inhibitor of USP7/HAUSP ubiquitin protease stabilizes and activates p53 in cells. *Mol Cancer Ther* **8**, 2286-2295 (2009).
34. Altun, M. *et al.* Activity-based chemical proteomics accelerates inhibitor development for deubiquitylating enzymes. *Chem Biol* **18**, 1401-1412 (2011).
35. Tian, X. *et al.* Characterization of selective ubiquitin and ubiquitin-like protease inhibitors using a fluorescence-based multiplex assay format. *Assay Drug Dev Technol* **9**, 165-173 (2011).
36. Wu, J. *et al.* Chemical Approaches to Intervening in Ubiquitin Specific Protease 7 (USP7) Function for Oncology and Immune Oncology Therapies. *J Med Chem* (2017).
37. Ndubaku, C. & Tsui, V. Inhibiting the deubiquitinating enzymes (DUBs). *J Med Chem* **58**, 1581-1595 (2015).
38. Lee, J.G., Baek, K., Soetandyo, N. & Ye, Y. Reversible inactivation of deubiquitinases by reactive oxygen species in vitro and in cells. *Nat Commun* **4**, 1568 (2013).
39. Wrigley, J.D. *et al.* Enzymatic characterisation of USP7 deubiquitinating activity and inhibition. *Cell Biochem Biophys* **60**, 99-111 (2011).

40. Winter, A. *et al.* Biophysical and computational fragment-based approaches to targeting protein-protein interactions: applications in structure-guided drug discovery. *Q Rev Biophys* **45**, 383-426 (2012).
41. Kessler, B.M. Selective and reversible inhibitors of ubiquitin-specific protease 7: a patent evaluation (WO2013030218). *Expert Opinion on Therapeutic Patents* **24**, 597-602 (2014).
42. Lor, L.A. *et al.* A simple assay for detection of small-molecule redox activity. *J Biomol Screen* **12**, 881-890 (2007).
43. Ritorto, M.S. *et al.* Screening of DUB activity and specificity by MALDI-TOF mass spectrometry. *Nat Commun* **5**, 4763 (2014).
44. Tovar, C. *et al.* MDM2 small-molecule antagonist RG7112 activates p53 signaling and regresses human tumors in preclinical cancer models. *Cancer Res* **73**, 2587-2597 (2013).
45. Wang, S. *et al.* SAR405838: an optimized inhibitor of MDM2-p53 interaction that induces complete and durable tumor regression. *Cancer Res* **74**, 5855-5865 (2014).
46. Vogelstein, B. HAUSP is Required for p53 Destabilization. *Cell Cycle* **3**, 689-692 (2004).
47. Emsley, P., Lohkamp, B., Scott, W.G. & Cowtan, K. Features and development of Coot. *Acta Crystallogr D Biol Crystallogr* **66**, 486-501 (2010).
48. Murshudov, G.N.*e.a.* Refinement of macromolecular structures by the maximum-likelihood method. *Acta Crystallogr D Biol Crystallogr* **53**, 240-255 (1997).
49. Adams, P.D. *et al.* PHENIX: a comprehensive Python-based system for macromolecular structure solution. *Acta Crystallogr D Biol Crystallogr* **66**, 213-221 (2010).
50. Bochevarov, A.D. *et al.* Jaguar: A high-performance quantum chemistry software program with strengths in life and materials sciences. *International Journal of Quantum Chemistry* **113**, 2110-2142 (2013).

**FIGURE LEGENDS**

**Figure 1: High-resolution X-ray co-crystal structure of USP7 in complex with 2 (PDB accession number 5N9R)**. a, Overall structure of USP7 in complex with **2** (2.2 Å resolution). The catalytic triad is highlighted in green. Compound **2** is shown in an orange space filling representation. Ubiquitin aldehyde (from PDB structure 1NBF) is included as a magenta ribbon for reference (position determined by sequence and structural alignment with 1NBF). b, Ribbon and stick representation showing the key interactions between USP7 and **2**. The intramolecular CH-π interaction between piperidine *C*-3 axial hydrogen and the aromatic group is also shown. c, Co-crystal structure of USP7 with **2** overlaid with the C-terminal region of ubiquitin (gold) illustrating how **2** partially protrudes into the channel normally occupied by the Ub tail creating a steric clash with the ubiquitin C-terminus.

**Figure 2**: **High-resolution X-ray crystal structure of USP7 in complex with 4 (PDB accession number 5N9T)**. a, Structure solved at 1.7 Å resolution. Ribbon and stick representation showing the key interactions between USP7 and **4** including the interaction with Q351, the adjacent water molecules and the various potential hydrogen bonds (predicted interaction energy magnitude ≥ 0.5 kcal/mol, distance cutoff 4.5 Å) between **4**, F409 and R408. b, Overlay of the structures of Compounds **2** and **4** in complex with USP7.

**Figure 3: Selectivity profile of 3 against a panel of DUBs.** a, Representative selectivity profile of **3** against a panel of 21 USPs and 17 other DUBs (DUBprofiler™, Ubiquigent). Screening was performed at a fixed concentration of 100 μM against all other members of the USP/DUB family. All data reported as the mean of 2 independent experiments.

**Figure 4: Target engagement and selectivity profile of 3 against selected USPs in cells.** a, Cells (HCT116) were treated with **3** and ***ent*-3** for 2 h (as indicated), lysed and the ubiquitin-propargylamine (Ub-PA) probe was added. Samples were subsequently analysed by western blotting probing for USP7 (quantitative analysis shown from 2 independent experiments). b, No target engagement (HCT116 cells) was detected up to 50 μM against the most closely related USP7 family member (USP47). Similar results were obtained when probing against additional non-related USPs including USP4, 11, 19. (+) and (–) signs represent the presence or absence of the Ub-PA probe. Concentration (Conc.). Full blots and cut membranes are shown in **Supplementary Figures 16a, b**.

**Figure 5: Treatment of cells with 3 caused non-genotoxic stabilisation of p53 and decreased levels of MDM2.** a, HCT116 cells were treated with **3**, ***ent*-3** and SAR405838 for 2 h and lysed for western blotting analysis probing for USP7, p53, pSer15-p53, p21, MDM2 and β-actin as indicated. b, Repeat of (a) in the MCF7 (breast adenocarcinoma) cell line. Western blotting analysis was performed as

described previously. The proteasome inhibitor MG132 was used at a concentration of 10 µM. Full blots and cut membranes are shown in **Supplementary Figures 16c, d**. c, Quantitative determination of ubiquitinated MDM2 in SJSA-1 cell line. Cells were treated with increasing concentration of inhibitors for 24 h (as indicated). Assay and analysis was performed as recommended by the manufacturer's instructions (MSD). Signal (A.U.) represents the ratio of ubiquitinated MDM2 normalised to total levels of MDM2. Data reported as the mean of at least three independent experiments with standard deviations.

## TABLES

**Table 1: Chemical structures and compiled data for USP7 binding fragments and inhibitors.**

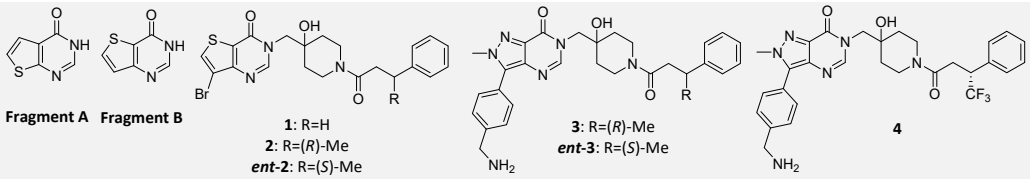


| Assays | 1 | 2 | *ent*-2 | 3 | *ent*-3 |
|---|---|---|---|---|---|
| **Redox** [a] | free | free | free | free | free |
| **Kinetic solubility (µM)** | >200 | >200 | >200 | >200 | >200 |
| **USP7 $IC_{50}$ (µM) – FP assay** | 13.1±0.8 | 0.3±0.1 | 46.0±5.6 | 0.006±0.002 | 2.4±0.3 |
| **USP7 $IC_{50}$ (µM) – Ub-Rh110** | 15.1±1.4 | 0.3±0.07 | >50 | 0.0015±0.001 | 1.9±0.4 |
| **SPR Kd (µM)** | 7.7±0.1 | 2.6±0.1 | >50 | 0.002±0.001 | 5.0±0.1 |
| **SPR $k_{off}$ ($s^{-1}$)** | 0.25±0.01 | 0.03±0.001. | 0.47±0.01 | 0.0004±0.0001 | 0.09±0.01 |
| **DUB selectivity**[c] | - | 0/18 | - | 0/38 | - |
| **Target engagement $EC_{50}$ (µM)** [b] | >50 | 0.85±0.15 | >50 | 0.049±0.025 | >50 |
| **Ub-MDM2 $EC_{50}$ (µM)** [b] | >20 | 2.6 | >20 | 0.055±0.015 | >20 |

Chemical structures, biochemical, biophysical profiling of USP7 inhibitors. Upper panel: chemical structures of the inhibitors (as indicated). Primary hit finding was performed by SPR using the Beactica fragment library. See Online Methods Section and main text for more details on these assays. Enantiomer (*ent*-); [a] redox free: free of redox cyclic activity when tested up to 200 µM; fluorescence polarisation (FP). [b] 50 and 20 µM were the maximum concentration used. – not determined. [c] number of DUBs showing >20% inhibition at 100µM / total number of DUBs tested. Data reported is the mean of at least 3 independent experiments ± standard deviations.

ONLINE METHODS

**Materials and reagents**

All reagents and chemicals were purchased from Sigma-Aldrich unless otherwise stated. The MDM2 antagonists nutlin-3a (Tocris, #3984), SAR405838 (MedchemExpress; MI-773, #HY-17493) and RG7112 (MedchemExpress, #HY-10959) were purchased from commercial suppliers as indicated and used with no further purification. All inhibitors were prepared as 10 mM DMSO stocks for cell culture experiments and stored in a controlled environment using the MultiPod system. CellTiter-Glo® was purchased from Promega (#G7571). The ubiquitin-propargylamine (Ub-PA) probe was purchased from UbiQ (#UbiQ-057). Unless otherwise stated, all other reagents were obtained from commercial sources and used without further purification.

**Compound synthesis and characterisation**

Compound synthesis and characterisation data are included in the **Synthetic Procedures Section**.

**Cell lines and culture conditions**

All cell lines were obtained from the American Type Culture Collection (ATCC), authenticated by STR profiling (Promega) and shown to be mycoplasma-free using the MycoAlert mycoplasma detection (Lonza; LT07-318). For growth, cells were maintained at 37°C in a humidified atmosphere with 5% $CO_2$. HCT116 (colorectal) cells were cultured in McCoys 5A supplemented with 10% (v/v) FBS, 1% (v/v)

Penicillin/streptoMycin, 1% (v/v) L-Glutamine. RS4;11 (acute lymphoblastic leukemia), LNCaP (prostate) and SJSA-1 (osteosarcoma) cells were cultured in RPMI supplemented with 10% (v/v) FBS, 1% (v/v) Penicillin/streptoMycin, 1% (v/v) L-Glutamine. MCF7 (breast) cells were cultured in Eagle's Minimum Essential Medium supplemented with 10% (v/v) FBS, 0.01 mg/mL human recombinant insulin and 1% (v/v) Penicillin/streptoMycin. Medium and supplements were purchased from Life Technologies except where indicated.

**Biochemical assay and reversibility studies**

USP7 activity was monitored in a fluorescence polarisation (FP) homogeneous assay using the isopeptide ubiquitin-Lys-tetramethylrhodamine substrate (Ub-TMR; U-558, Boston Biochem). Full-length USP7 was purchased from Boston Biochem (His6-$USP7_{FL}$, E-519). Unless otherwise stated, all other reagents were purchased from Sigma. Enzymatic reactions were conducted in black flat bottom polystyrene 384-well plates (Nunc) in 30 µL total volume. USP7 (2.5 nM, 10 µL) was incubated in assay buffer containing 50 mM HEPES (pH 7.2), 150 NaCl, 0.5 mM EDTA, 5 mM DTT, 0.05% BSA (w/v), 0.05% CHAPS in the presence or absence of inhibitor (10 µl). Inhibitors were stored as 10 mM DMSO stocks in an inert environment (low humidity, dark, low oxygen, room temperature) using the Storage Pod System and serial dilutions were prepared in buffer just prior to the assay (typically from 200 to 0.001 µM in 10 dp curve). Following incubation at room temperature for 30 min, the enzymatic reactions were initiated by dispensing the Ub-TMR substrate (250 nM, 10 µL). FP was measured every 15 min over a period of 90 min (within the linear range of the assay) using a Synergy 4 plate reader (BioTek) exciting at 530 nm and measuring the

amount of parallel and perpendicular light at 575 nm. The FP signal was subsequently normalised to the no compound control (i.e. DMSO). Analysis and $IC_{50}$ values were derived using GraphPadPrism (GraphPad Software, Inc, La Jolla, CA; four-parameter logistic function). All data presented as mean ± s.d. (n >=3). For the 100x dilution assay, USP7 was pre-incubated for 30 min with 10x the inhibitor $IC_{50}$ value followed by 100x dilution. USP7 activity was assessed 15 min post-dilution as described above. Ubiquitin, iodoacetamide (#A3221; Sigma-Aldrich) and $H_2O_2$ were used at a final pre-dilution concentration of 150 µM, 1.0 mM and 0.001 % solution respectively.

**Redox assay**

The property of small molecule to oxidise the target was assessed using the method described by Lor *et al*[42]. Briefly, compounds at a final assay concentration of 200 µM were incubated for 30 min in buffer containing 50 mM HEPES (pH 7.5), 50 mM NaCl, plus 5 µM Resazurin (#R7017; Sigma-Aldrich) and 50 µM DTT, in a black low volume 384-well Greiner plate. Readout was performed with Excitation of 560 nm and Emission of 590 nm using a Synergy 4 plate reader (BioTek). Data was normalised to the no DTT control.

**SPR experiments**

Residues S207 to E560 of the USP7 catalytic domain (CD) was expressed in E.coli cells using a p10T7-2 expression vector with an N-terminus His6-GST tag cleavable with TEV protease. The purified protein stored in a PBS solution was immobilised on a

$COOH_5$ SensiQ chip by amine coupling at a concentration of 150 µg.ml$^{-1}$ and a pH = 4.5 Na-Acetate solution to achieve a Rmax of approximately 100 RU, for a 500 g.mol$^{-1}$ small molecule under saturation conditions (i.e. above 10-fold $K_d$). The SensiQ Pioneer surface plasmon resonance (SPR) system was equilibrated with a HBS-EP buffer solution (10 mM HEPES, 150 mM NaCl, 3 mM EDTA, 0.05 % P20 surfactant) with the addition of 5 % DMSO and 2 mM DTT on the day of the experiment. All samples were tested in the same buffer solution with 5% DMSO and 2 mM DTT with an association injection time of 75 µl.min$^{-1}$ and a 60 s dissociation time under a 3 % sucrose gradient. Data was analysed using Qdat v 2.5.2.12. from SensiQ Technologies, Inc. unless otherwise stated.

**Mode of inhibition**

Compound **3** at final assay concentrations ranging from 25 µM to 0.78 nM was pre-incubated for 30 min with 5 nM of full-length USP7 (2.5 nM final assay concentration). Five microliters of ubiquitin-aminocumarin (Ub-AMC; # 60-0116-050; Ubiquigent) was added at varying concentrations ranging from 1.5 nM to 25 µM to a final assay volume of 15 µl in low volume black 384-well plates (Greiner # 784076). Fluorescence intensity (ex = 350 nm, em = 445 nm) was measured over 90 min and initial linear rates were calculated. Global fit analysis for competitive models were performed using GraphPadPrism (GraphPad Software, Inc, La Jolla, CA; Global fit Michaelis-Menten enzyme inhibition). $IC_{50}$ values were also determined at increasing concentration of Ubiquitin-AMC representing the substrate concentration at 1-fold, 10-fold and 50-fold the $K_M$ of ubiquitin-AMC for USP7 using a Synergy 4 plate reader

(BioTek). Data analysis was performed using GraphPadPrism (GraphPad Software, Inc, La Jolla, CA; four-parameter logistic function).

**F-Test**

Global fitting models for each mode of inhibition; competitive, non-competitive and uncompetitive, were subject to an F-Test statistical analysis to further confirm the mode of inhibition. The F-Test compares the fit between two different equations. The lower $Chi^2$ indicates the fit between two models is significantly better. The $Chi^2$ values for the competitive, non-competitive and uncompetitive models were respectively; 1352.6, 572.8 and 3307.1. A significant probability should be lower than 0.05. The non-competitive model gives the best statistical fit with the lowest $Chi^2$ and a probability of 1.0 $e^{-12}$ in accordance with the visual interpretation. The results of the F-Test analysis are summarised in **Supplementary Table 2**.

**Protein Production, Crystallisation, data collection and structure determination**

The USP7 catalytic domain (residues 207-560) genetically fused with a C-terminal hexa-histidine tag was expressed in E.coli. BL21 cells were transformed with the corresponding expression plasmid and grown in Terrific broth (TB) and protein expression induced with 0.25 mM IPTG overnight at 16°C. After harvesting by centrifugation, cell pellets were resuspended in Lysis Buffer (40 mM TRIS-HCl, 500 mM NaCl, 1 mM AEBSF, 2 mM TCEP, 5 mM Imidazole, 0.1% Tween 20, pH 7.5) and lysed by sonication on ice. The soluble fraction was then loaded directly onto an IMAC column (5 mL HisTrap HP) pre-equilibrated with Lysis Buffer and the protein eluted with IMAC Buffer B (40 mM TRIS-HCl, 500 mM NaCl, 1 mM AEBSF, 2 mM

TCEP, 300 mM Imidazole, 0.1% Tween 20, pH 7.5). Fractions containing the desired protein were pooled and buffer exchanged by disalysis (MWCO 8,000-10,000 Da) against anion exchange (AEX) Buffer A (20 mM TRIS-HCl, 30 mM NaCl, 1 mM EDTA, 4 mM DTT, pH 8.0). The protein was then loaded onto a YMC-BioPro ion exchange column (15 x 120, 7.4 ml) pre-equilibrated with AEX Buffer A and eluted over 30 CV with a gradient of 0-50% AEX Buffer B (20 mM TRIS-HCl, 1M NaCl, 1 mM EDTA, 4 mM DTT, pH 8.0). Fractions were analysed by SDS-PAGE and those containing the desired protein were pooled and then further purified by SEC (HighLoad Superdex 75 column) using a running buffer of 10 mM TRIS-HCl, 100 mM NaCl, 4 mM DTT, pH 8. SEC fractions were analysed by SDS-PAGE and the pure fractions pooled and concentrated (Vivaspin column, MWCO 12KDa) to 5.3 mg / ml as measured by UV $A_{280nm}$.

Crystals of USP7 in complex with inhibitors were grown by hanging drop vapour diffusion. For the USP7/**2** complex, a 14.2 mg/ml solution of USP7 (10 mM TRIS-HCl, 100 mM NaCl, 4mM TCEP) at pH 8.0 was pre-incubated with a 5.9-fold molar excess of **2** (50 mM in DMSO) for 3 h. 0.7 µl of the protein solution was then mixed with 0.7 µl of reservoir solution containing 100 mM TRIS-HCl (pH 7.75), 200 mM Li2-Sulfate, 29% (w/v) PEG4000 and equilibrated at 4°C over 0.4 ml of reservoir solution. For the USP7/**4** complex, a 14.2 mg/ml solution of USP7 (10 mM TRIS-HCl, 100 mM NaCl, 4mM TCEP) at pH 8.0 was pre-incubated with an 8.9-fold molar excess of **4** (150 mM in DMSO) for 3 h. 2 µl of the protein solution was then mixed with 2 µl of reservoir solution (100 mM TRIS-HCl (pH 8.5), 200 mM Li2-Sulfate, 28% (w/v) PEG 4000) and equilibrated at 20°C over 0.4 ml of reservoir solution.

Diffraction data at 2.23 Å resolution for a USP7/**2** crystal was collected with a Bruker MicroStar rotating anode generator equipped with Osmic optics. The structure was solved via molecular replacement using the PDB entry 1NB8 as a template. Iterative manual modelling in Coot[47] and refinement using REFMAC5[48] resulted in the final model. 97% of backbone torsions for the final model are within the Ramachandran favoured regions, with 3% in the allowed regions. Diffraction data at 1.7 Å resolution for a USP7/**4** crystal was collected at the ESRF synchrotron radiation source, id30a1, Grenoble. The structure was solved via molecular replacement using the USP7/**2** structure as a template. Iterative manual modelling in Coot and refinement using REFMAC5 resulted in the final model. 96% of backbone torsions for the final model are within the Ramachandran favoured regions, with 4% in the allowed regions. The crystallography data collection and refinement statistics are provided in **Supplementary Table 1.** Composite omit maps were calculated in Phenix[49]; ligand atoms were removed and mFo-DFc omit maps generated using the phenix.composite_omit_map tool and are shown in **Supplementary Figures 5c** and **6b**. The atomic co-ordinates and structure factors for the USP7/**2** and USP7/**4** complex structures have been deposited in the PDB under accession codes 5N9R and 5N9T respectively.

**Computational Chemistry**

Images were created using Molecular Operating Environment (MOE, 2016.0802; Chemical Computing Group ULC, 1010 Sherbooke St. West, Suite #910, Montreal,

QC, Canada, H3A 2R7 (2017)) and Maestro (Schrödinger Release 2016-4: Maestro, Schrödinger LLC, New York, NY (2016)

### *Ab-initio* calculations

*Ab-initio* quantum mechanical calculations to determine the relative strain induced by rotation of the phenyl ring were performed in Jaguar[50]. In order to simplify the calculation and eliminate the effect of interactions between the phenyl ring and the piperazine, the ligand from the USP7/compound **2** complex was truncated and reproduced in both the *(R-)* and *(S-)* stereoisomers (**Supplementary Figure 4**). The geometries of both the *(R-)* and *(S-)* forms of the truncated ligand were optimized in Jaguar using a B3LYP/6-31G** basis set and the default optimisation settings. The dihedral angle between the phenyl ring and the methyl carbon attached to the adjacent chiral centre was manually adjusted to reflect the orientation of the phenyl ring observed in the crystal structure (37.7° between the phenyl and methyl for the active *(R-)* stereoisomer and 151.3° for the inactive *(S-)* stereoisomer). Single point energy calculations were then performed for each stereoisomer in Jaguar, using the B3LYP/6-31G** basis set and default settings.

### Selectivity assays

Selectivity assays were performed against all DUBs available in the DUBprofiler™ panel (n=39 in total; Ubiquigent). Screening was performed at a fixed inhibitor

concentration of 100 µM. Data generated is displayed as a percentage inhibition of total enzyme activity for each enzyme. Of note, USP47 was not part of the DUBprofiler™ panel at Ubiquigent and so was not tested biochemically. Selectivity against the protease (n=63) and kinase (SelectScreen; n=49) panels were performed at Reaction Biology and Life Technologies respectively using a fixed inhibitor concentration of 10 µM. Data generated is displayed as a percentage inhibition of total enzyme activity for each enzyme. All data presented as mean ± s.d. (n >=2).

**Target engagement assay**

HCT116, LNCaP or RS4;11 cells were treated with vehicle (DMSO) or USP7 inhibitors for 2 h. Following incubation, cells were washed extensively thrice with 1x PBS and harvested in TE lysis buffer containing 50 mM TRIS-HCl (pH7.4), 150 mM NaCl, 5 mM $MgCl_2$, 0.5 mM EDTA, 0.5% NP40, 10% Glycerol, 2 mM DTT and clarified cell lysates (40 µg) incubated with the ubiquitin-propargylamine probe (Ub-PA; 8 µg/ml final concentration) in assay buffer containing 50 mM TRIS-HCl (pH7.6), 5 mM $MgCl_2$, 250 mM Sucrose, 0.5 mM EDTA, 2 mM DTT for 30 min. The reaction was terminated by the addition of LDS sample buffer (Life Technologies) and heated to 70°C. Samples were then analysed by western blotting using the Cell Signalling anti-USP7 Ab (#4833; 1/1000 dilution). $EC_{50}$ values were determined upon densitometry analysis. Band intensities were quantified using ImageJ software where the upper bands (USP7-Ub) and lower bands (USP7) were calculated as a percentage of the corresponding DMSO controls (-/+ Ub-PA) and values were then normalised to the sum of the lower and upper bands for each concentration. Selectivity was assessed

using the Cell Signalling anti-USP4 (#2651, 1:1000), anti-USP11 (#GTX101446, 1:1000), anti-USP30 antibodies (#ab189518; 1:1000) and the Santa Cruz anti-USP47 antibody (#sc-100633, 1:500).

**Cellular activity assay and western blotting**

In order to assess the cellular activity of the compounds, HCT116 or MCF7 cells were treated with compounds or vehicle (DMSO) for a period of 2 h. Cells were subsequently harvested, lysed in radioimmuno-precipitation (RIPA) buffer containing 50 mM TRIS-HCl (pH 7.6), 150 mM NaCl, 1 mM EDTA, 1.0% NP40, 0.25% Na-deoxycholate and supplemented with a phosphatase (PhosSTOP, Roche) and protease inhibitor cocktail tablet (complete Mini, Roche). For the timecourse experiments, LnCaP and RS4;11 cells were treated with inhibitors as indicated and harvested at 8, 24, 48 and 72 h. Western blotting analyses were carried out using antibodies purchased from Cell Signalling; anti-USP7 (#4833; 1:1000 dilution), anti-Ser15p53 (#9284; 1:1000), anti-PARP (#9542, 1:1000), anti-cleaved Caspase 3 (#9664; 1:1000), Santa Cruz; anti-p53 (#sc-263; 1:500), Millipore; anti-MDM2 (#OP46; 1:200), anti-p21 (#05-345; 1:1000), Sigma; anti-β-actin (#A5316; 1:2000), HRP conjugated anti-rabbit (#A0545; 1:5000) and HRP conjugated anti-mouse (#A9917; 1:5000).

**MDM2 ubiquitination assay (MSD)**

SJSA-1 cells were seeded in 96 well plate format and treated with vehicle (DMSO) or inhibitors as indicated for 24 h. 7 dp titration curves were typically used from 10 pM to 20 µM in 1 log unit increments. Cells were then lysed and the total protein

concentrations determined with the BCA protein kit assay (ThermoFischer Scientific; #23227). Detection of the ubiquitinated and total MDM2 protein levels was performed using the MDM2 whole cell lysate kit as recommended by the manufacturer's instructions (# K15168D; Meso Scale Discovery). Data was acquired on a MesoQuickPlex SQ120 reader. Results were normalised to the total MDM2 protein concentration and $EC_{50}$ values derived using GraphPadPrism (GraphPad Software, Inc, La Jolla, CA; four-parameter logistic function). Data presented as mean $\pm$ s.d. (n >=3).

**MDM2 ubiquitination levels (western blot)**

LNCaP cells were seeded in 100 mm dishes to achieve a confluency of 70-90% the following day. 10 µg of HA-tagged ubiquitin plasmid was transfected per plate using Lipofectamine 2000 (ThermoFischer), at a Lipofectamine:DNA ratio of 1:4. Media was replenished after 6 h and cells were harvested 48 h post-transfection. Cells were treated with **3** and ***ent*-3** for 45 min to 1.5 h (as indicated). Protein G Sepharose beads (GE Healthcare) were stored in a 25% slurry in ethanol at 4◦C. Immediately prior to use, 0.5 mL was aliquoted, centrifuged at 1000 x g and washed twice in 1 mL lysis buffer. Beads were then suspended in 1 mL RIPA lysis buffer and incubated with 50 µg anti-MDM2 (#Ab-1, Merck) 2 h at 4◦C. The beads were then pelleted by centrifugation, resuspended in fresh lysis buffer and aliquoted between lysate samples (750 µg protein). The volume of each sample was normalised with lysis buffer and samples were allowed to incubate for 4 h. Beads were then washed 4 times in 1 mL lysis buffer in a succession of spin-resuspension cycles and boiled in 50

µL LDS sample buffer to dissociate bound proteins, prior to SDS-PAGE. Samples were analysed by western blotting using the anti-HA antibody (Thermo Scientific, 1:2000).

**Cell proliferation assay**

Cells were seeded in 96 well plate format (typically 2500 cells/well for MCF7, LNCaP, SJSA-1 and 5000 cells/well for the RS4;11 line) and treated after 24 h with increasing concentrations of compound (typically in a 9 dp curve ranging from 31 µM to 1.25 nM). Cell viability was assessed by CellTiter-Glo® using a Synergy 4 plate reader (BioTek) after 72 h (RS4;11) or 6 days (LNCaP, SJSA-1) as recommended by the manufacturer's instructions (Promega; # G7571). Analysis and $EC_{50}$ values were derived using GraphPadPrism (GraphPad Software, Inc, La Jolla, CA; four-parameter logistic function). Data presented as mean ± s.d. (n >=3).

**Data Availability Statement**

Structural data that support the findings of this study have been deposited in the RCSB Protein Data Bank (PDB, www.rcsb.org) with the accession numbers 5N9R and 5N9T. The authors declare that all other data supporting the findings of this study are available within the paper (and its Supplementary Information files).

**Statistics and reproducibility**

The data reported in this study represent the mean and standard deviation of at least 3 independent experiments as specified in the Figure legend (unless otherwise stated; **Figure 3**). For the mode of inhibition study, an F-test statistical analysis was

performed as described in details in the Online methods and **Supplementary Table 2**.

**SUPPLEMENTARY INFORMATION - Figures**

**Supplementary Figure 1**

**a**

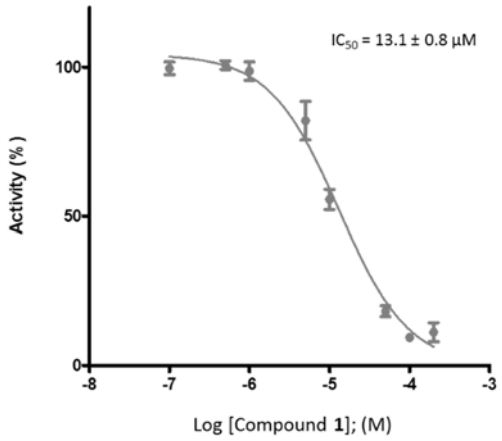


**b**

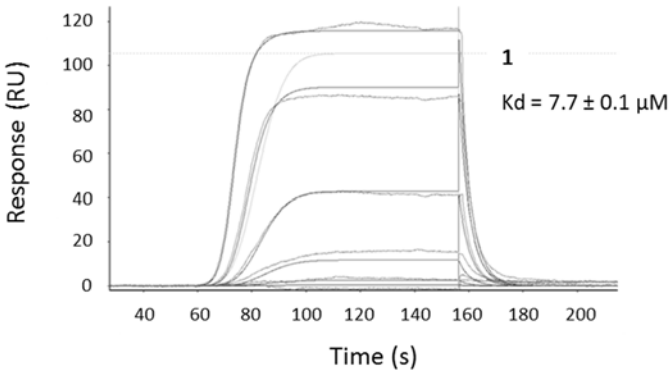


**c**

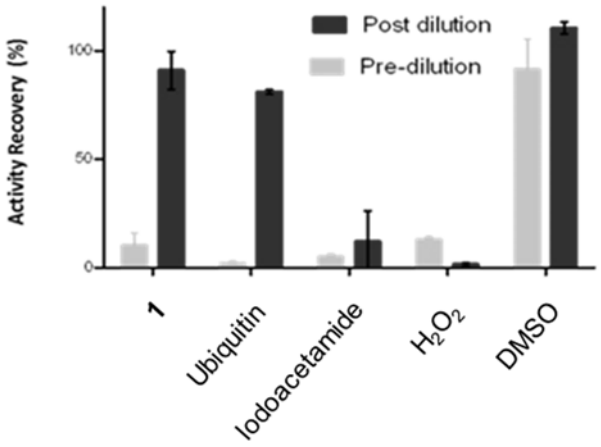

**Supplementary Figure 1: Biochemical characterisation and binding validation of the reversible USP7 inhibitor 1.** a, Biochemical inhibition of USP7 by **1**. Activity was monitored using the full-length protein and the Ub-TMR isopeptide substrate. b, Representative orthogonal binding validation. Binding of **1** was confirmed by SPR with representative titration sensorgrams shown for inhibitor concentration of 0, 0.8, 4.0, 20.0 and 100.0 µM (data summarised in **Table 1**). c, Reversible binding demonstrated by high-dilution assay. Assay controls included ubiquitin, iodoacetamide and $H_2O_2$. DMSO: no compound control using the same DMSO final concentration for treatment with **1**. Data reported as the mean of at least 3 independent experiments with standard deviations.

**Supplementary Figure 2**

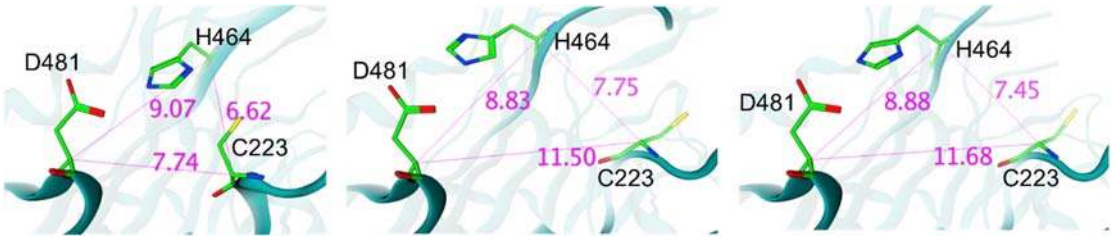


1NBF Ub bound | USP7:**2** co-crystal structure | 1NB8 *apo*

**Supplementary Figure 2: USP7 catalytic site and misaligned triad (H464, C223 and D481).** Inter-residue distances are shown in Å. Left: USP7-Ub bound structure (1NBF), showing the properly aligned triad; middle: USP7 co-crystal structure with **2**, showing a misaligned triad (the co-crystal structure with **4** has an essentially identical arrangement, with 0.27 Å pairwise RMSD between the triad residues); right: USP7 *apo* structure (1NB8), showing a similarly misaligned catalytic triad.

**Supplementary Figure 3**

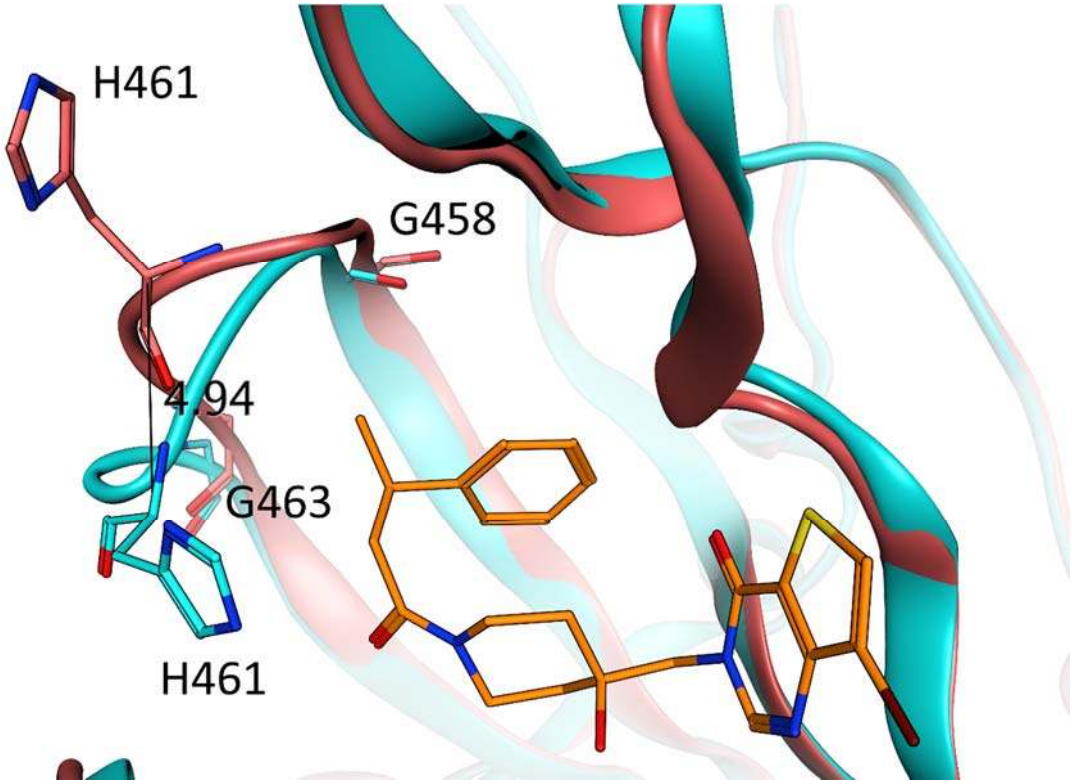


**Supplementary Figure 3: Diagram showing the conformational change of the loop between Gly458 and Gly463 in response to binding of 2.** The loop folds in towards the ubiquitin binding channel positioning His461 between the ligand and the catalytic cysteine. This results in a movement of 4.94 Å as indicated.

**Supplementary Figure 4**

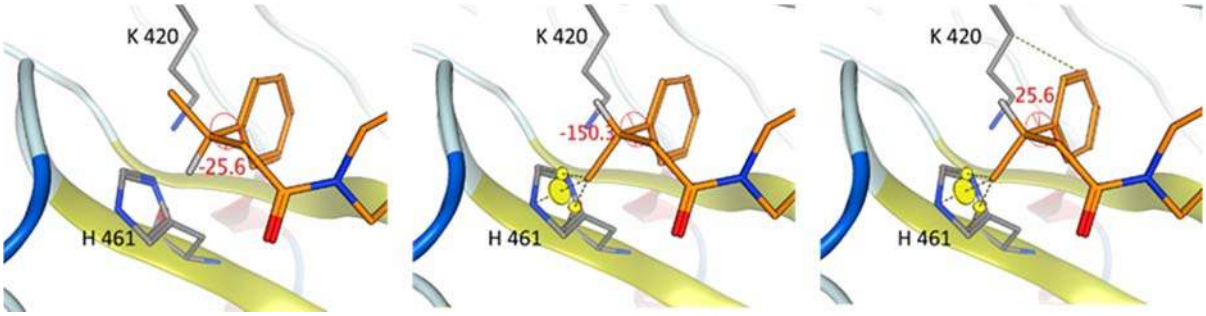

**Supplementary Figure 4: Rationale for the enantioselective binding of 2 (vs *ent*-2) to USP7.** Left: co-crystal structure of USP7 with **2**. Middle: ***ent*-2** cannot bind in an analogous conformation to **2** due to a steric clash with H461 and internal strain induced by movement of the phenyl ring further out of the plane of the C-H bond from the chiral centre. Right: Rotation of the phenyl ring cannot completely ameliorate the internal strain due to a steric clash with K420. Areas of steric clash are indicated by yellow circles and dotted lines. See main text and Online Methods section for details. The truncated ligand **7** used in the *ab-initio* strain calculations is shown below.

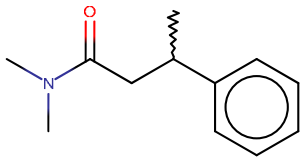


**7**

**Supplementary Figure 5**

**a**

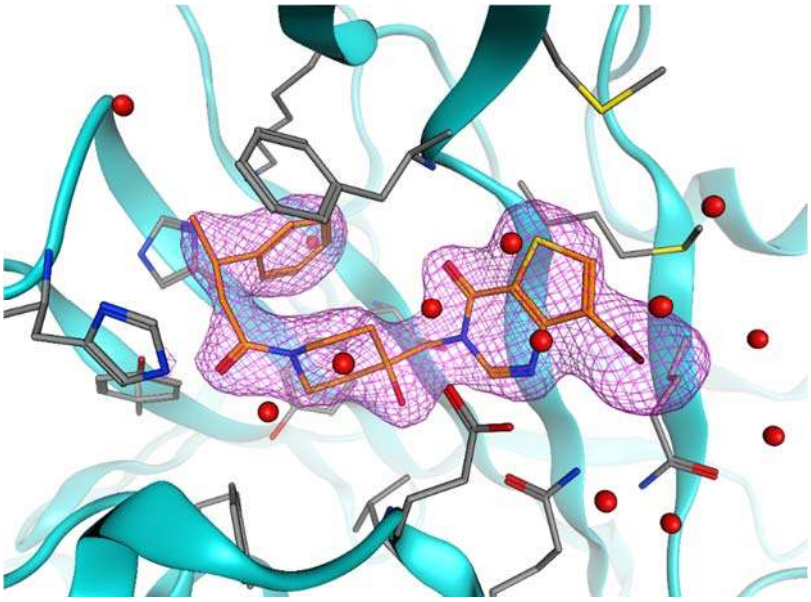

**b**

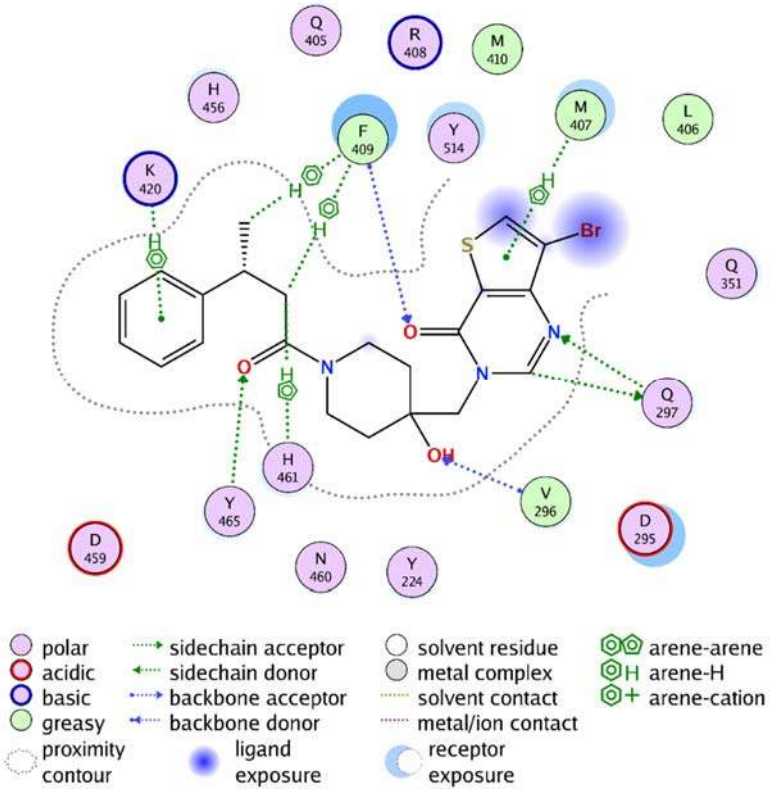

**c**

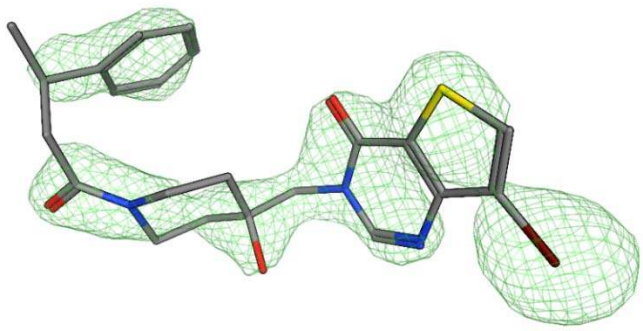

**d**

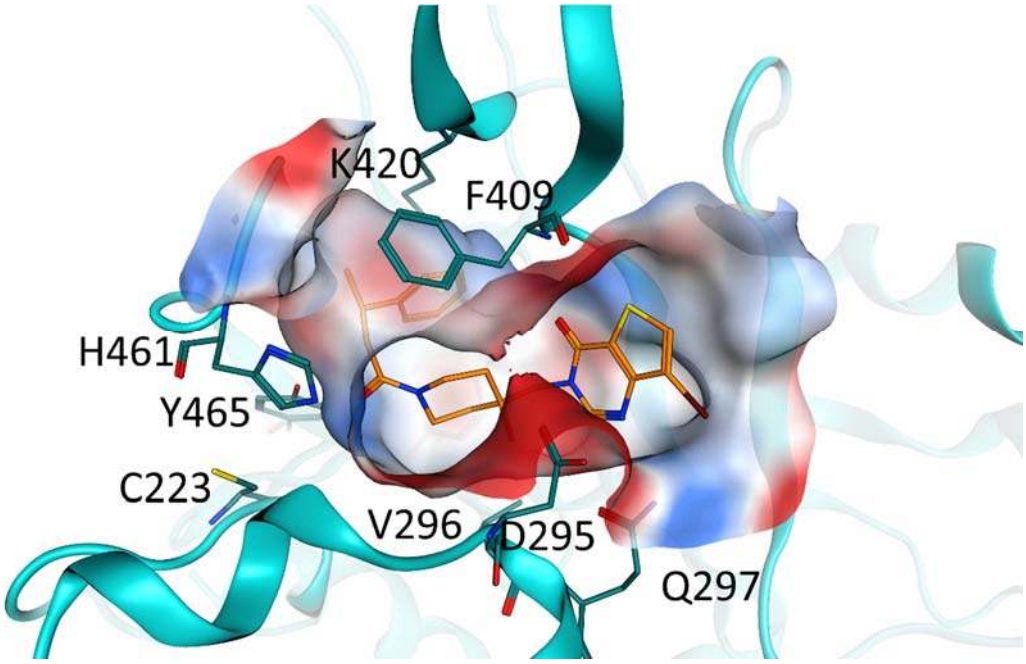

**Supplementary Figure 5: Electron density, 2D plot, omit and surface charge maps for 2 in complex with USP7.** a, 2mFo-DFc 2σ difference map of **2** in complex with USP7**.** b, 2D interaction plot of **2** in complex with USP7. c, mFo-DFc 3σ composite omit map for **2** in complex with USP7. d, Map showing the surface charge around the binding pocket for **2** in complex with USP7.

**Supplementary Figure 6**

**a**

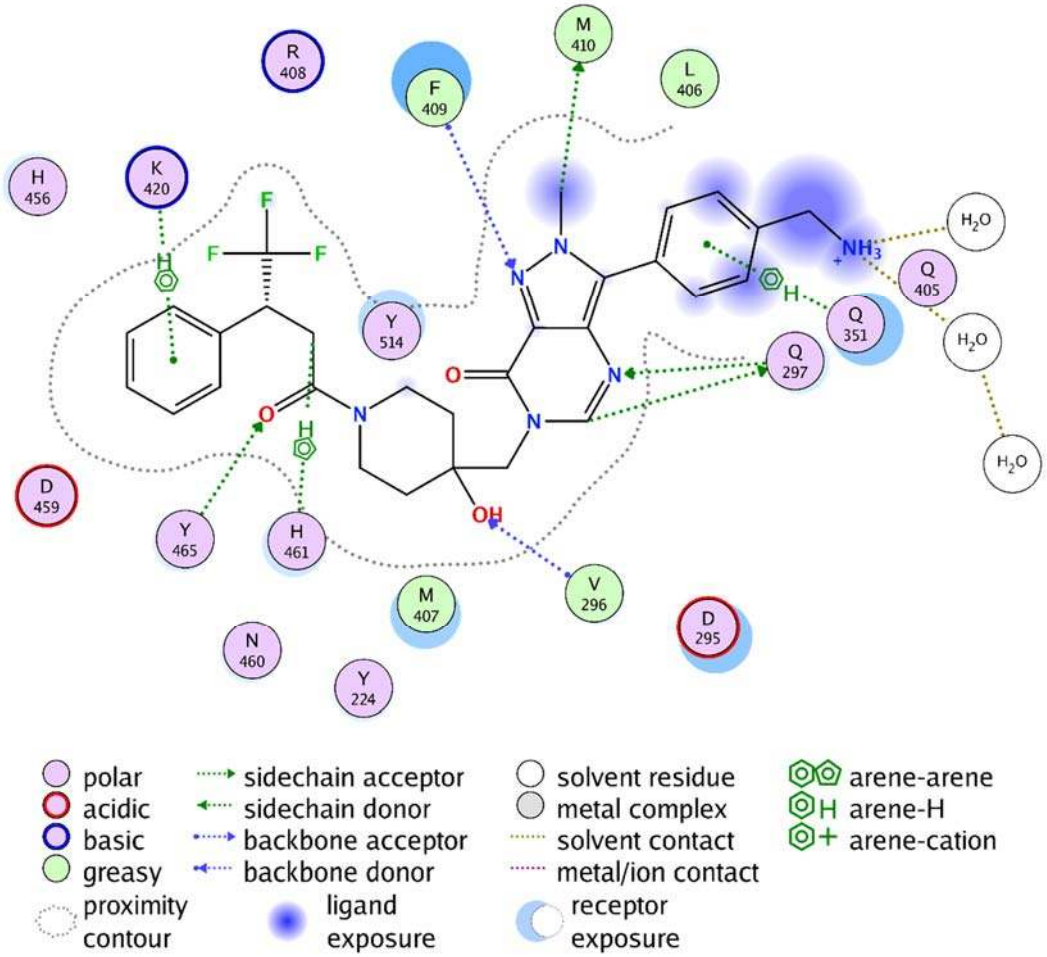

**b**

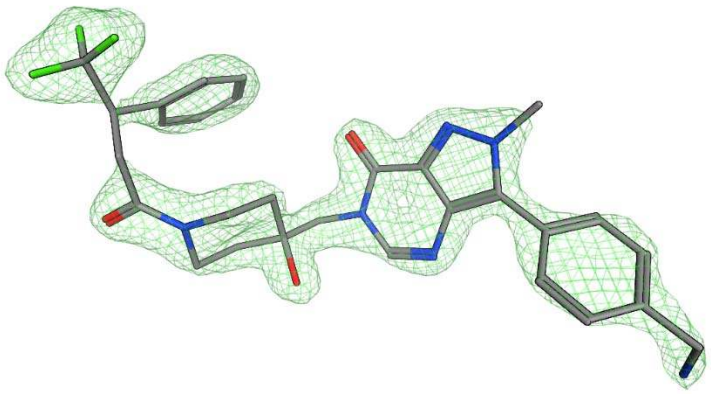

**c**

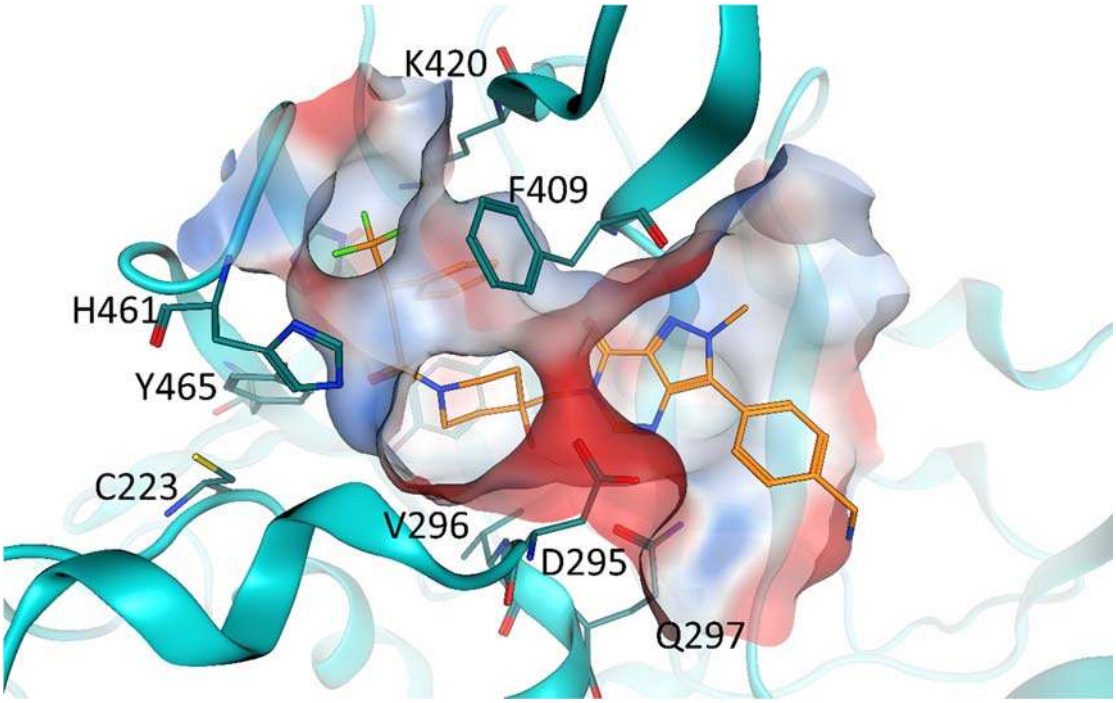


**Supplementary Figure 6: 2D plot, omit and surface charge maps for 4 in complex with USP7.** a, 2D interaction plot of **4** in complex with USP7. b, mFo-DFc 3σ

composite omit map for **4** in complex with USP7. c, Map showing the surface charge around the binding pocket for **4** in complex with USP7.

**Supplementary Figure 7**

**a**

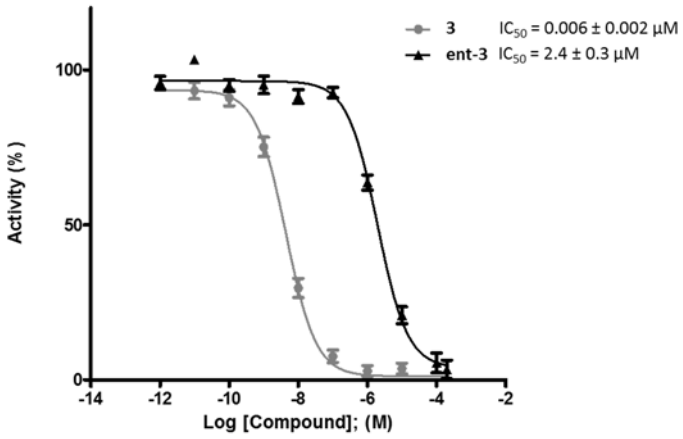


**b**

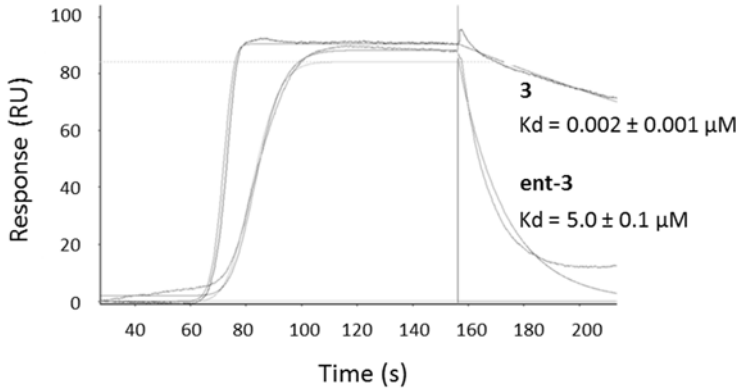

**Supplementary Figure 7: Development of highly potent USP7 inhibitors.** a, Biochemical inhibition of USP7 by **3** and its enantiomer ***ent*-3** (>400-fold difference in potency). Biochemical activity was monitored using the full-length protein and the Ub-TMR isopeptide substrate. b, Orthogonal characterisation and binding validation by SPR. Representative sensorgrams for **3** and ***ent*-3** are shown (data summarised in **Table 1**). Data reported as the mean of at least 3 independent experiments with standard deviations.

**Supplementary Figure 8**

**a**

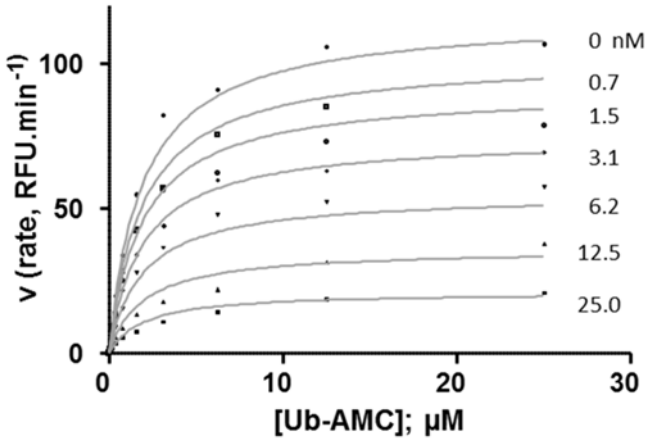


**b**

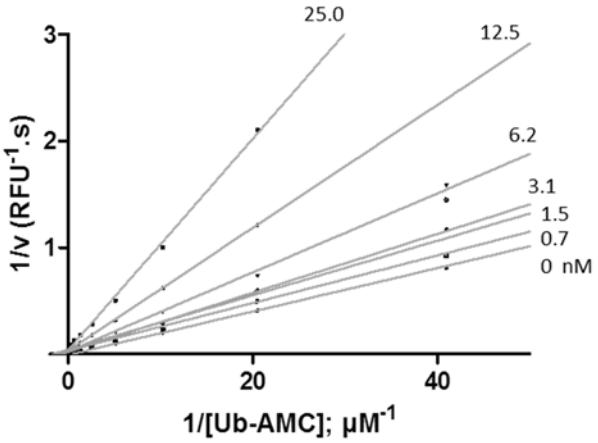

**c**

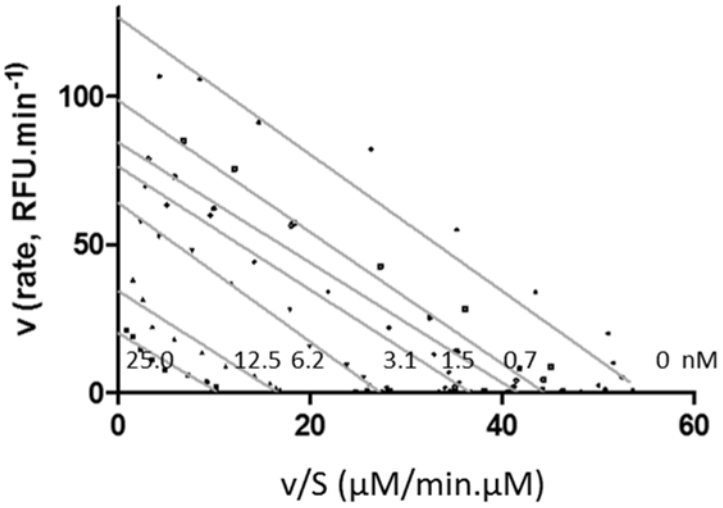


**Supplementary Figure 8: Characterisation of the mode of inhibition of USP7 by 3.** a, Representative Michaelis-Menten plot. Inhibition was performed as indicated using varying concentrations of Ub-AMC (from 0 to 25 µM) and inhibitor concentration (from 0 to 25 nM, as indicated). R-square values for fitting were >0.95 in all cases. b, Lineweaver-Burk plot (plotted using data from *A*). c, Eadie-Hofstee plot of USP7 inhibition by **3**. Results from *A* were plotted as *V*/[S] against *V* where *V* is the reaction velocity for the inhibitor concentrations and S is the Ub-AMC concentrations (as indicated). The slope of the plots (parallel lines indicative of unchanged $K_M$ values) reveal a non-competitive mode of inhibition. R-square values for fitting were >0.95 in all cases. F-Test statistical analysis shows the lowest $Chi^2$ of 572.9 for the non-competitive model and the best probability of $1.72E^{-12}$ (see **Supplementary Table 2**).

**Supplementary Figure 9**

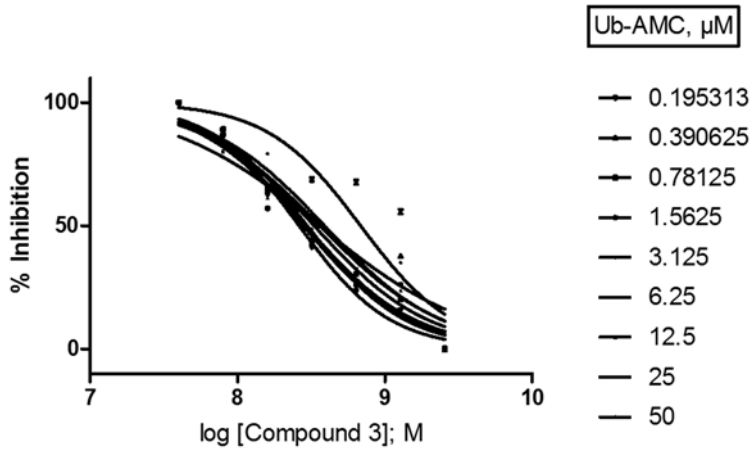


**Supplementary Figure 9: Biochemical inhibition of USP7 by 3 with increasing concentration of substrate.** Biochemical activity was monitored using the full-length USP7 protein and the Ub-AMC substrate using the concentration range as indicated. Analysis and $IC_{50}$ values were derived using GraphPadPrism (GraphPad Software, Inc, La Jolla, CA; four-parameter logistic function). Data represents the mean of 2 independent experiments.

**Supplementary Figure 10**

**a**

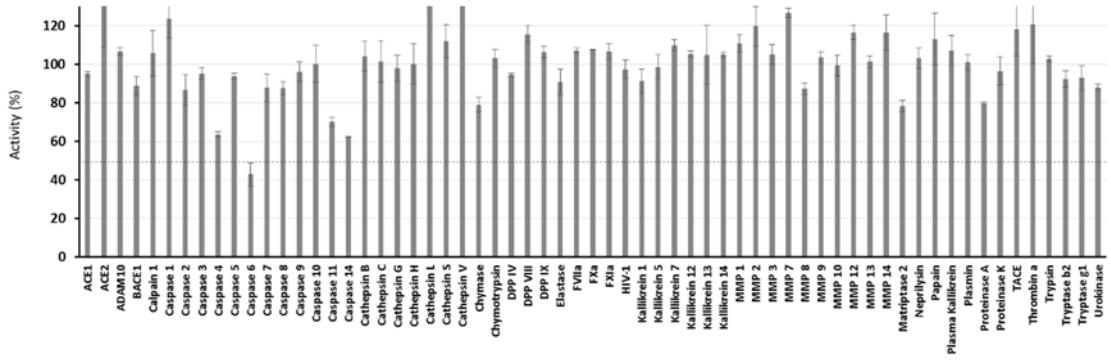

**b**

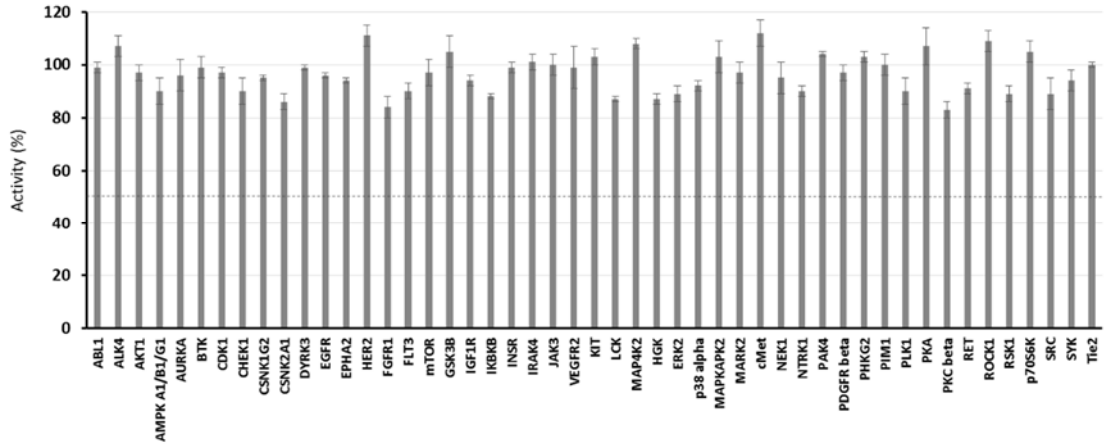


**Supplementary Figure 10: Selectivity profiles of Compound 3 against proteases and kinases.** a, Representative selectivity profile against the protease family. **3** was screened at 10 µM fixed concentration against a panel of 63 representative proteases across all family members including cysteine proteases (Reaction Biology). b, Representative selectivity profile against a panel of kinases. **3** was screened at 10 µM against a panel of 49 representative kinases (SelectScreen®, Life technologies). Data reported as the mean of at least two independent experiments with standard deviations.

**Supplementary Figure 11**

**a**

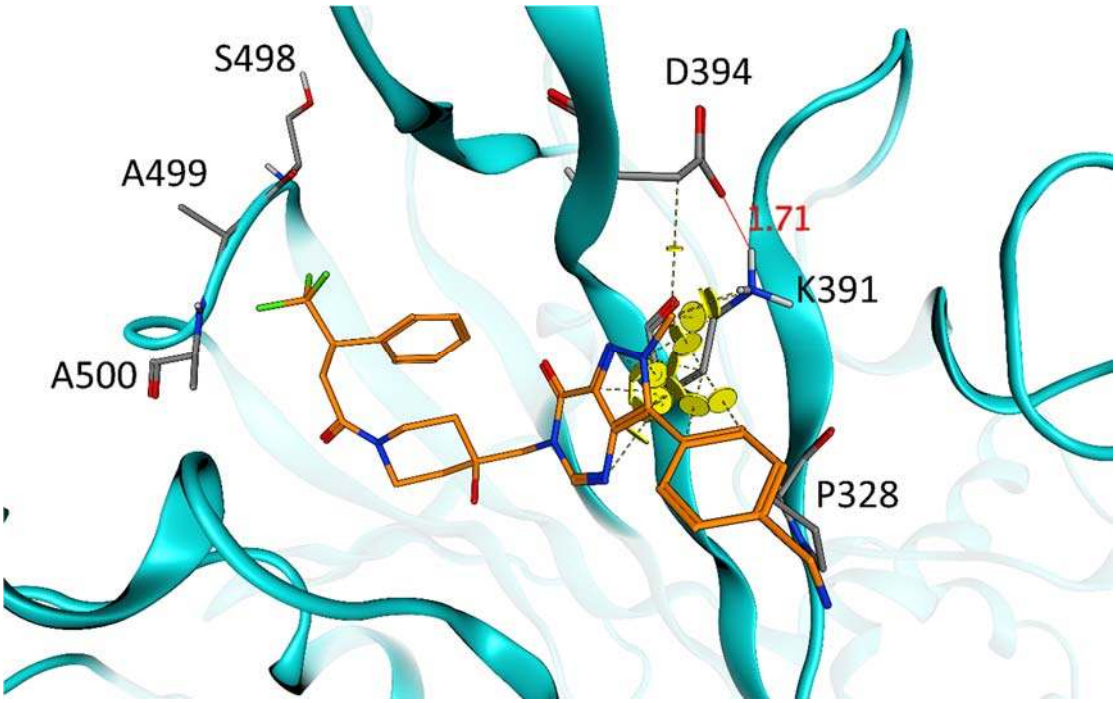


**b**

| USP7 residues | USP47 corresponding residues |
|---|---|
| Gln351 | Pro328 |
| Met407 | Lys391 |
| Met410 | Asp394 |
| Asp459 | Ser498 |
| Asn460 | Ala499 |
| His461 | Ala500 |

**Supplementary Figure 11: Binding selectivity of inhibitor for USP7 *vs* the closest homologue USP47.** a, Homology model of USP47 with the residues in the binding site which differ between USP47 and USP7 highlighted, leading to severe steric clashes with the USP7 ligands. The USP47 homology model was created in MOE. Residues 188-564 of Uniprot sequence Q96K76 were aligned to the co-crystal structure of USP7 and **4**. Fifteen main chain models were created, with 3 samples for each sidechain at 310 K, using the AMBER12:EHT force field. The bound ligand from the co-crystal structure was not included in the model and N-terminal and C-terminal outgaps were not modelled. Energy minimisation was applied to intermediate models and the final model, to a gradient of 1.0 and 0.5, respectively. The Protonate3D function was performed on the final model before minimisation. b, Table showing the 6 USP7 residues in the binding site situated within 5.0 Å of the ligand which differ in USP47 (as shown).

**Supplementary Figure 12**

**a**

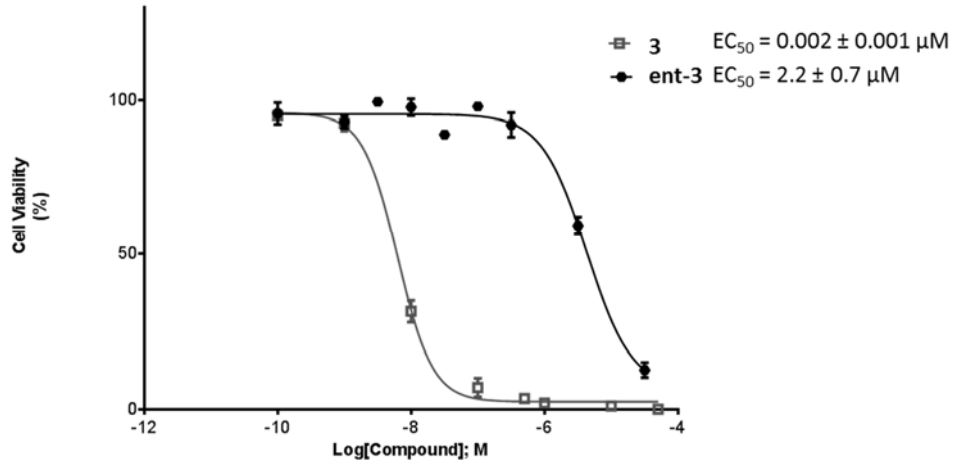

**b**

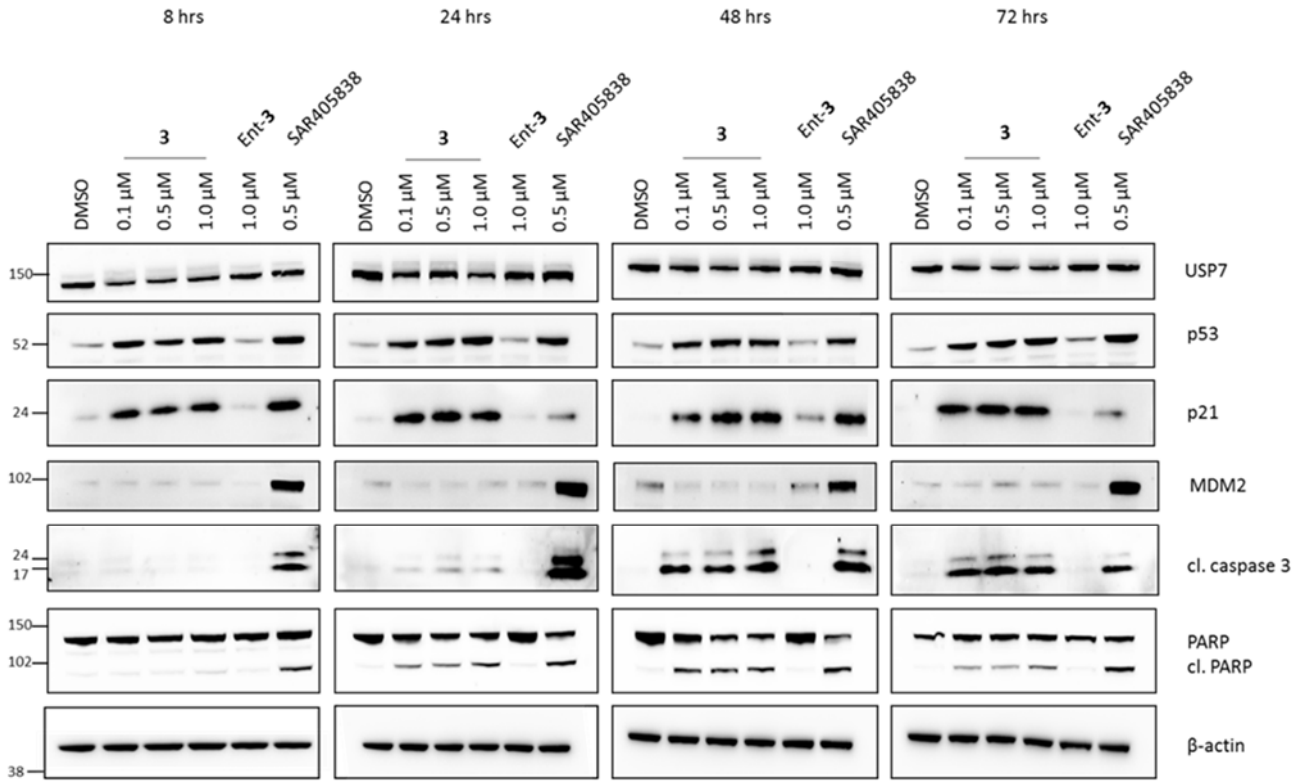
8 hrs
24 hrs
48 hrs
72 hrs
3
Ent-3
SAR405838
DMSO
0.1 μM
0.5 μM
1.0 μM
1.0 μM
0.5 μM
150
52
24
102
24
17
150
102
38
USP7
p53
p21
MDM2
cl. caspase 3
PARP
cl. PARP
β-actin

**c**

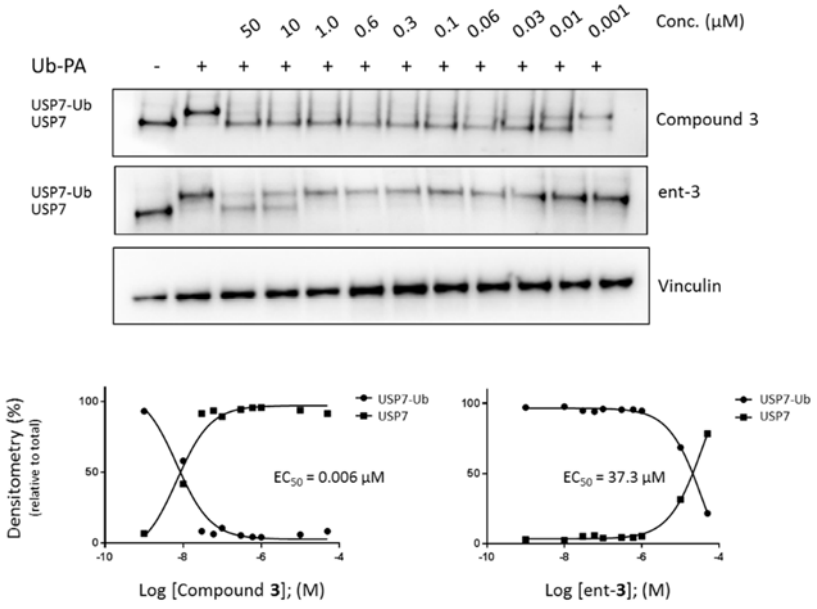
Conc. (μM)
50
10
1.0
0.6
0.3
0.1
0.06
0.03
0.01
0.001
Ub-PA
USP7-Ub
USP7
Compound 3
ent-3
Vinculin
Densitometry (%)
(relative to total)
EC50 = 0.006 μM
EC50 = 37.3 μM
Log [Compound 3]; (M)
Log [ent-3]; (M)

**Supplementary Figure 12: Characterisation of effects of 3 in RS4;11 cell line**

a, Anti-proliferative activity of **3** and ***ent*-3** in the RS4;11 cell line. Cellular viability was measured 72 h post treatment using the CellTiter-Glo® assay (Promega). Viability data reported as the mean of at least 3 independent experiments with standard deviations. $EC_{50}$ values compiled in **Supplementary Table 3**. b, Representative western blotting experiment in RS4;11 demonstrating the time-dependent apoptosis induction following treatment with the inhibitors (as indicated). c, Target engagement of **3** and ***ent*-3** in RS4;11 cells. Cells were treated with **3** and ***ent*-3** for 2 h (as indicated), lysed and the ubiquitin-propargylamine (Ub-PA) probe was added. Samples were subsequently analysed by western blotting probing for USP7. Densitometry and quantitative analyses were performed as described previously. Full blots and cut membranes are shown in **Supplementary Figure 16e**.

**Supplementary Figure 13**

**a**

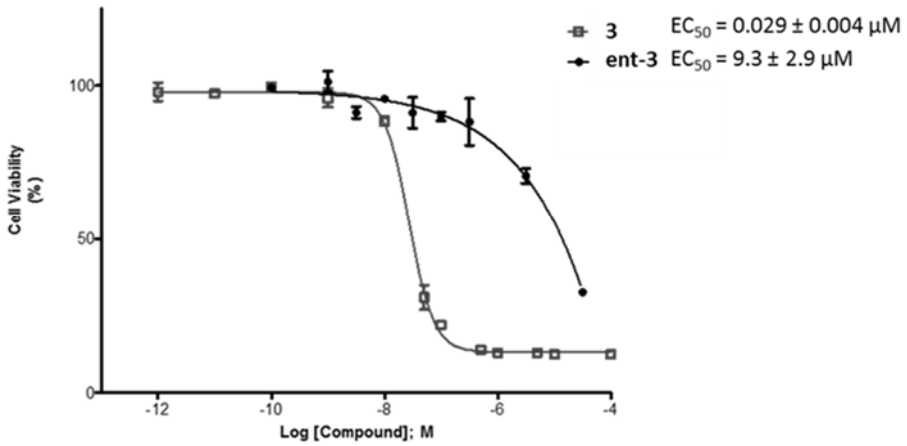

**b**

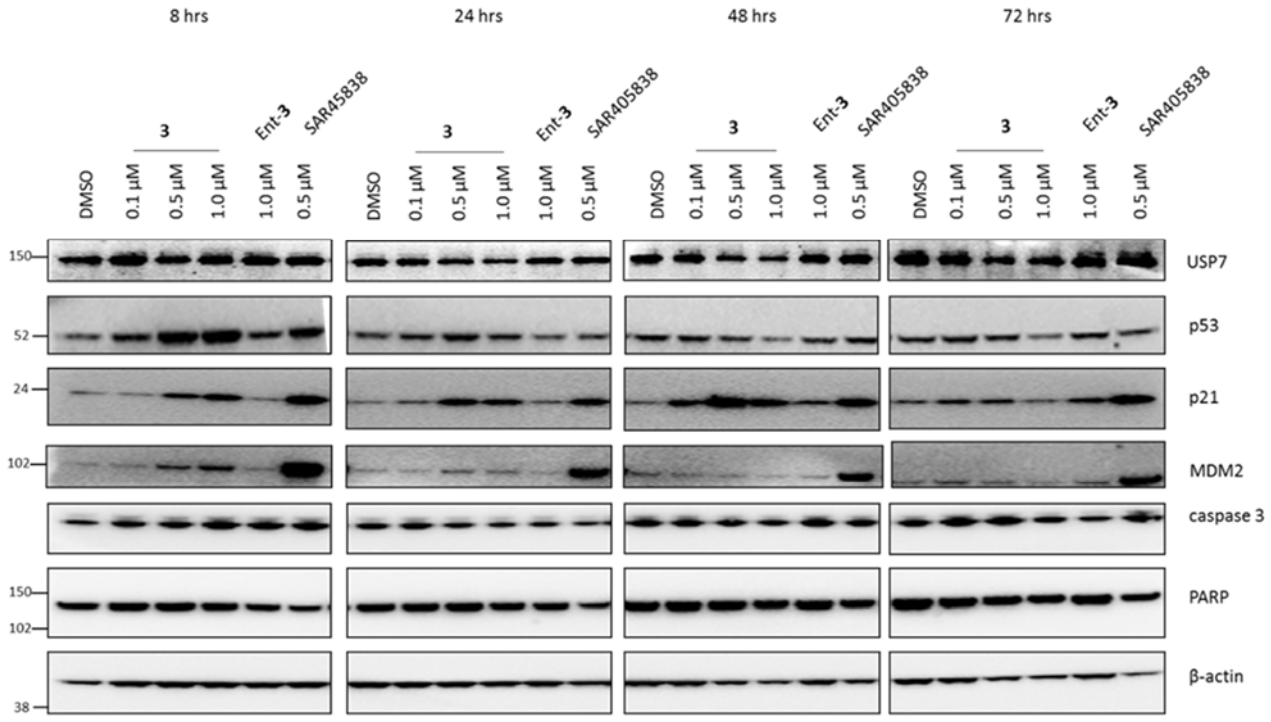
8 hrs
24 hrs
48 hrs
72 hrs
3
Ent-3
SAR405838
DMSO
0.1 μM
0.5 μM
1.0 μM
150
52
24
102
38
USP7
p53
p21
MDM2
caspase 3
PARP
β-actin

**c**

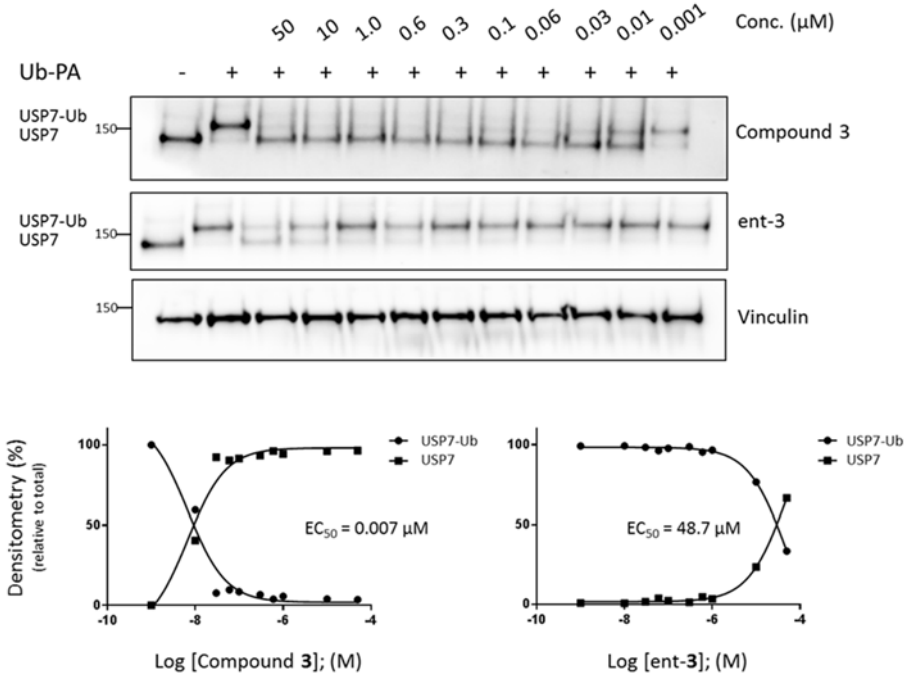
Conc. (μM)
50
10
1.0
0.6
0.3
0.1
0.06
0.03
0.01
0.001
Ub-PA
USP7-Ub
USP7
Compound 3
ent-3
Vinculin
Densitometry (%)
(relative to total)
EC50 = 0.007 μM
EC50 = 48.7 μM
Log [Compound 3]; (M)
Log [ent-3]; (M)

**d**

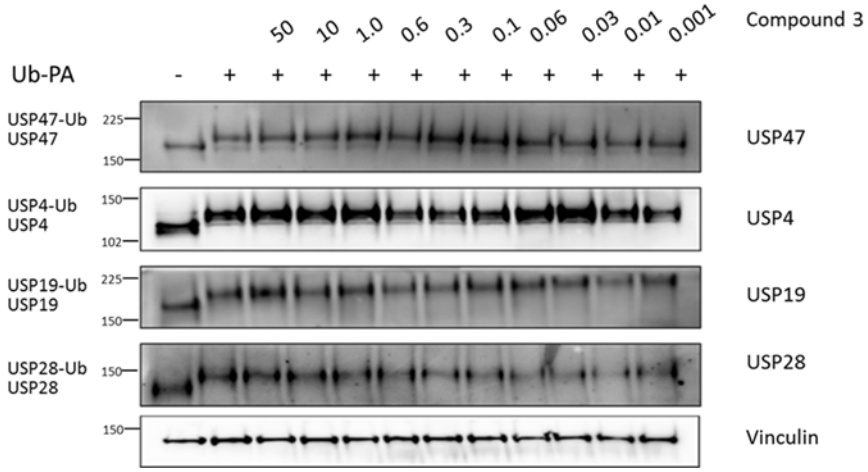


**e**

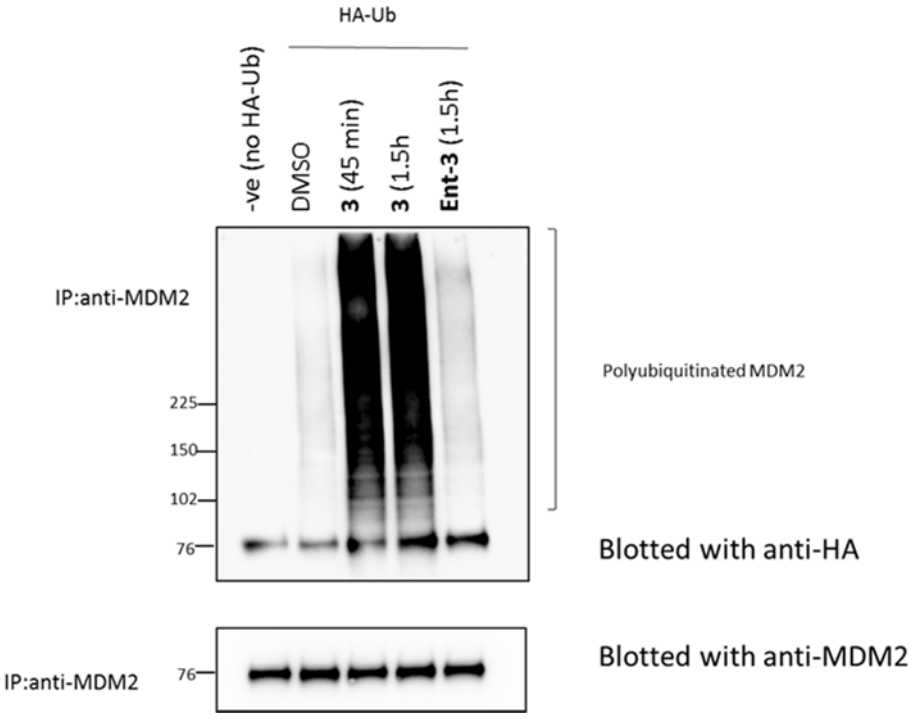


**Supplementary Figure 13: Characterisation of effects of 3 in LNCaP cell line.** a, Anti-proliferative effects demonstrated in solid tumor cell line (LNCaP). Cellular viability

was measured after 6 days as described previously. Viability data reported as the mean of at least 3 independent experiments with standard deviations. b, Representative western blotting analysis in the LNCaP cell line. Cells were treated with inhibitor as indicated. $EC_{50}$ values compiled in **Supplementary Table 3**. c, Target engagement: cells were treated with **3** and **ent-3** for 2 h (as indicated), lysed and the ubiquitin-propargylamine (Ub-PA) probe was added. Samples were subsequently analysed by western blotting probing for USP7. Densitometry analysis was performed for the upper (USP7-Ub) and lower (USP7) bands. Signal was subsequently normalised to the combined densitometry values for the upper and lower bands after background subtraction (quantitative analysis shown from 2 independent experiments). d, No target engagement was detected up to 50 μM against the most closely related USP7 family member (USP47). Similar results were obtained when probing against additional non-related USPs including USP4, 19, 28. (+) and (–) signs represent the presence or absence of the Ub-PA probe. Concentration (Conc.). e, Increased levels of MDM2 ubiquitination following treatment with **3**. HA-tagged ubiquitin (HA-Ub) was expressed in LNCaP cells. Cells were treated with 1.0 μM of compound or vehicle (as indicated) and MG132 (20 μM). Cells were lysed after 45 min or 1.5 h and MDM2 was immunoprecipitated from all samples. Western blotting analysis was performed using an antibody against the HA-tag (upper panel) or MDM2 (lower panel). Full blots and cut membranes shown in **Supplementary Figures 16f-h**.

**Supplementary Figure 14**

**a**

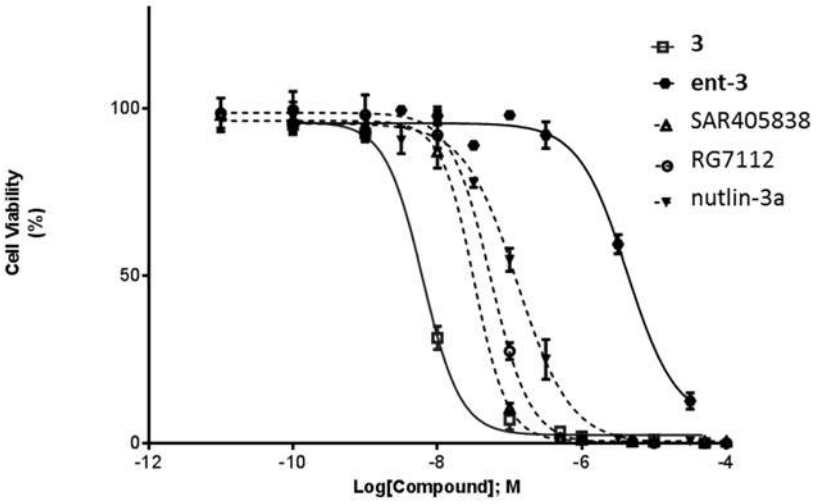


**b**

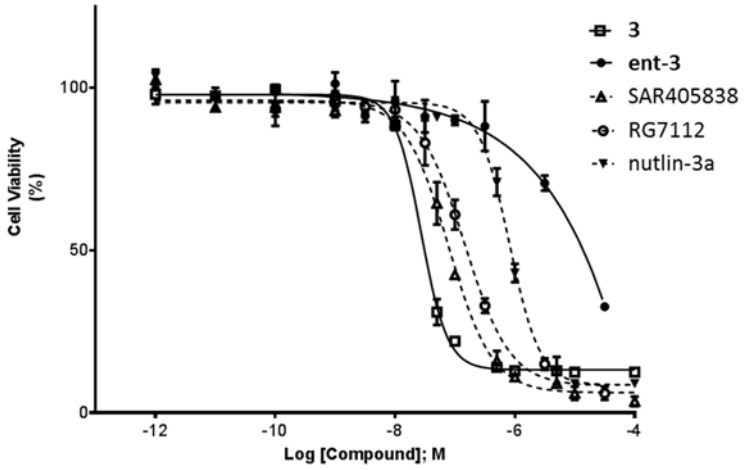


**c**

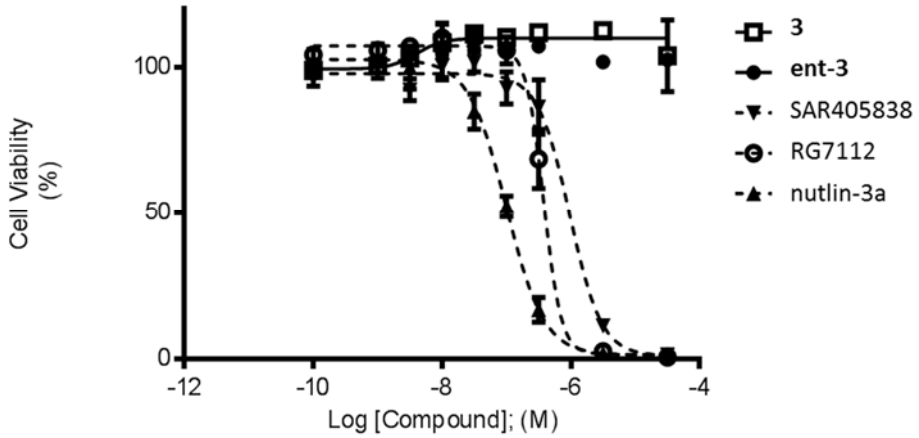


**d**

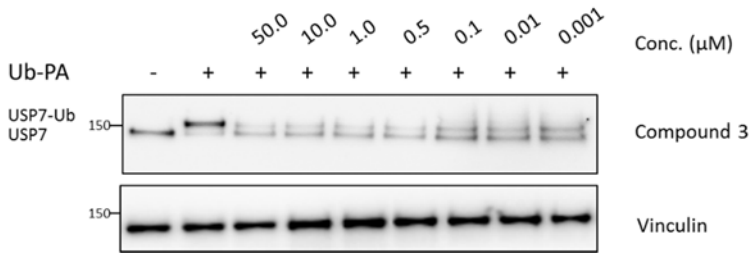


**Supplementary Figure 14: Direct benchmarking of 3 to MDM2 antagonists.** a, RS4;11 cells were treated with USP7 inhibitors or the MDM2 antagonists nutlin-3a, RG7112 and SAR405838 (as indicated). Cellular viability was measured after 72 h using CellTiter-Glo® (Promega) as described previously. b, Repeat of (a) in the LNCaP prostate cell line. Viability was assessed 6 days post treatment as described above. c, Differential activity between MDM2 antagonists and USP7 inhibitor in the osteosarcoma SJSA-1 cell line (as indicated). Viability was assessed 6 days post treatment as described before. Data reported as the mean of three independent experiments with standard deviations. All $EC_{50}$ values compiled in **Supplementary Table 3**. d, Target engagement in the SJSA-1 cell line. Full blots and cut membranes

are shown in **Supplementary Figure 16i**. The assay was performed as described previously for the HCT116 and LNCaP cell lines.

**Supplementary Figure 15**

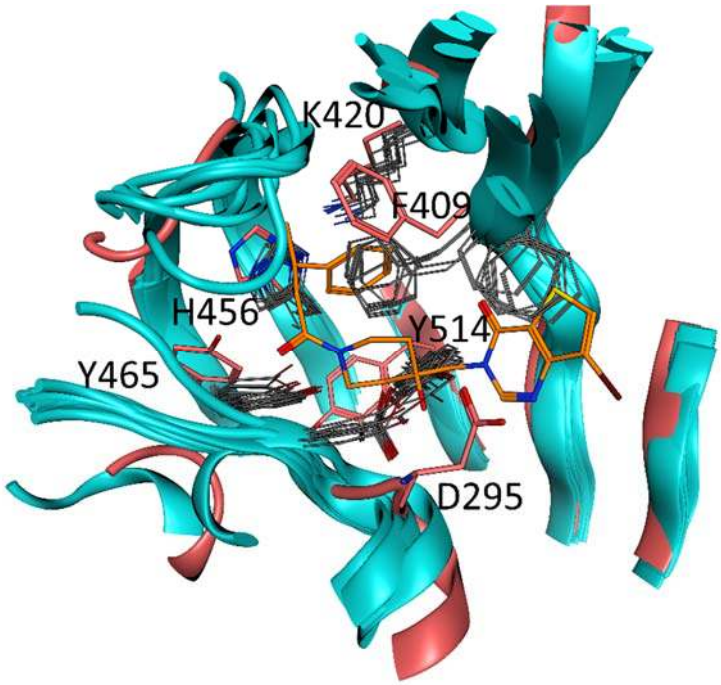


**Supplementary Figure 15: Comparison of the key residues forming the site for Compounds 2 and 4 with the equivalent residues from published crystal structures of other USPs.** USP7 is shown in salmon; other USPs (USP14, PDB 2AYN; USP8, PDB 2GFO; USP2, PDB 2IBI; USP4, PDB 2Y6E; USP21, PDB 3I3T; USP5, PDB 3IHP; USP2a, PDB 3NHE; USP18, 5CHT; USP46, PDB 5CVM; USP12, PDB 5K16) in cyan and grey. **2** is shown in orange. The key binding residues involved in binding which are indicated on the diagram are conserved in each of the USP's. Significant alterations in sidechain conformation are observed for some residues, particularly F409, which is observed in two different positions for the published structures

depending on whether the USP is in an *apo* state or in complex with ubiquitin. However neither of these clusters overlay precisely with the position of F409 in the current structure. Y514 also adopts a novel conformation in the current structure when in complex with the inhibitors reported here, compared to that observed in other published USP crystal structures. The position of D295 deviates from that of the equivalent residues in other USPs. This is due to the unusual activation mechanism of USP7, in which a conformational change in the switching loop (residues 285-291) is required for ubiquitin binding. Compounds **2** and **4** bind to the inactivated state of USP7, in which this conformational change has not occurred.

**Supplementary Figure 16**

**a**

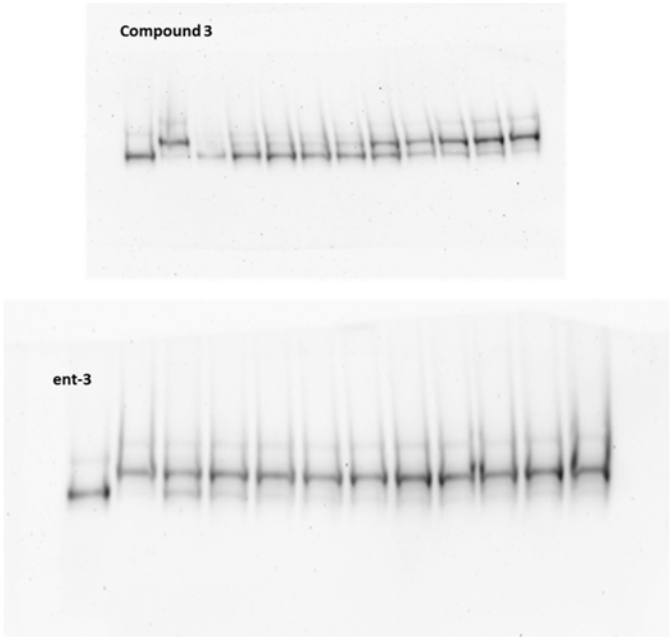

**b**

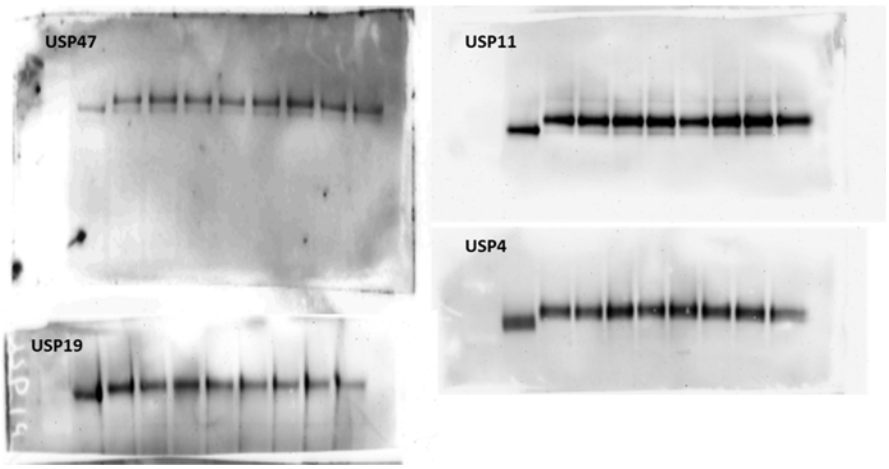
USP47
USP11
USP4
USP19

**c**

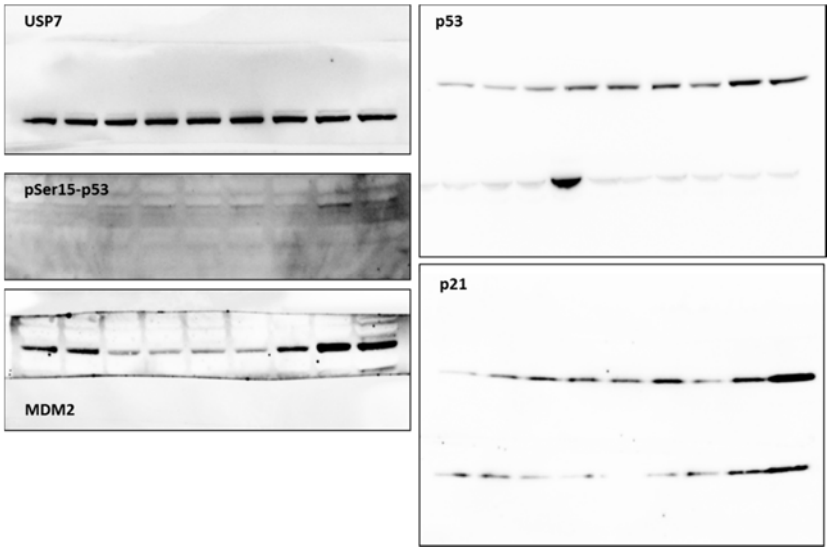
USP7
p53
pSer15-p53
p21
MDM2

**d**

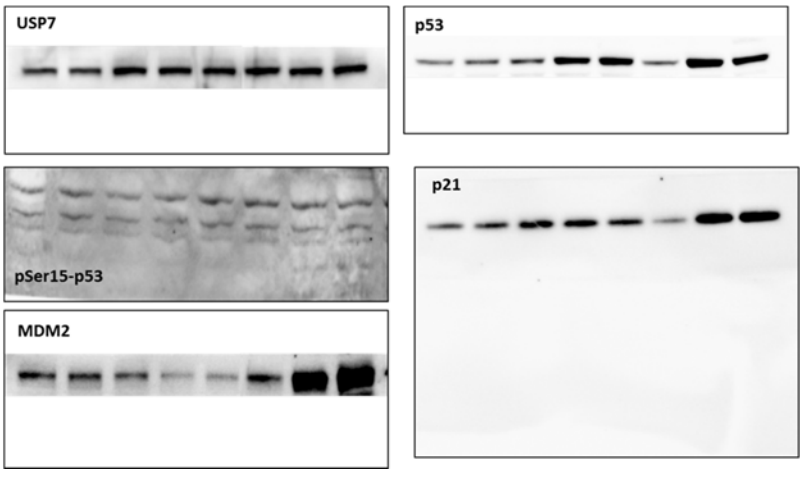
USP7
p53
pSer15-p53
p21
MDM2

**e**

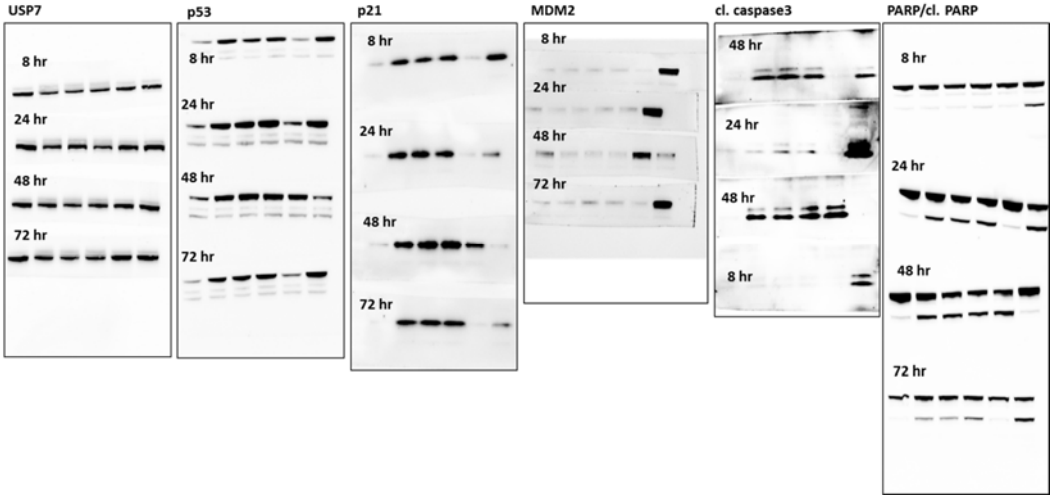
USP7
8 hr
24 hr
48 hr
72 hr
p53
8 hr
24 hr
48 hr
72 hr
p21
8 hr
24 hr
48 hr
72 hr
MDM2
8 hr
24 hr
48 hr
72 hr
cl. caspase3
48 hr
24 hr
48 hr
8 hr
PARP/cl. PARP
8 hr
24 hr
48 hr
72 hr

**f**

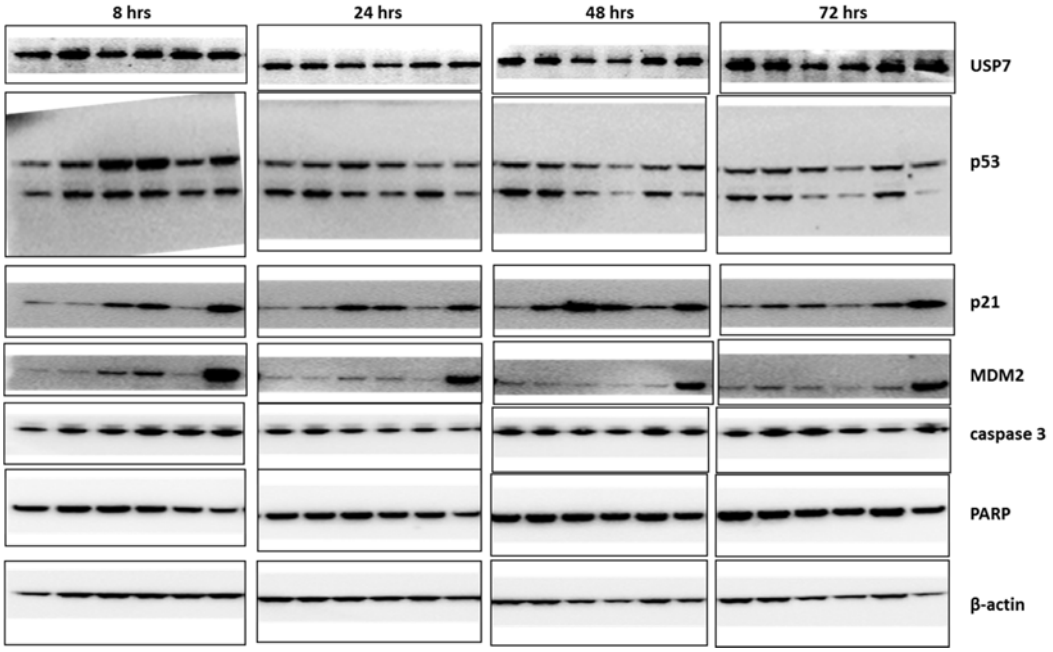
8 hrs
24 hrs
48 hrs
72 hrs
USP7
p53
p21
MDM2
caspase 3
PARP
β-actin

**g**

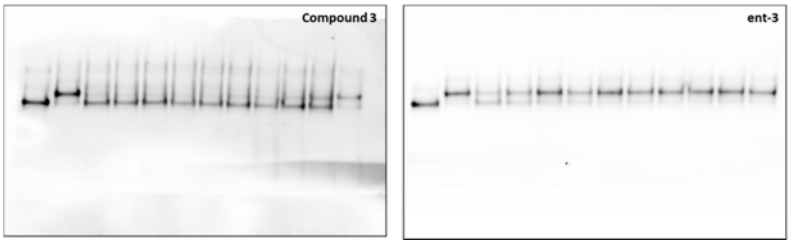
Compound 3
ent-3

**h**

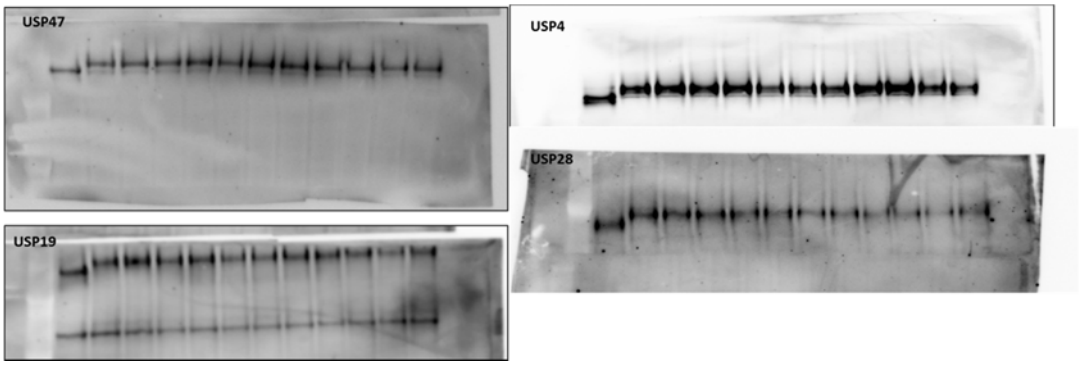


**i**

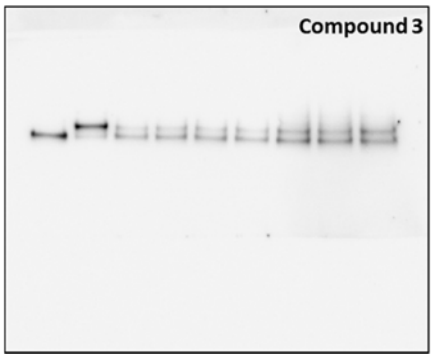


**Supplementary Figure 16: Full western blots or cut membranes.** a, Target engagement in HCT116 cell line (from **Figure 4a**). b, Selectivity profile against various DUBs in HCT116 cell line (from **Figure 4b**). c, Western blotting in HCT116 cell line corresponding to **Figure 5a**. d, Western blotting in MCF7 cell line corresponding to **Figure 5b**. e, Western blotting in RS4;11 cell line corresponding to **Supplementary Figure 12b** (timepoint as indicated). f, Western blotting in LNCaP cell line corresponding to **Supplementary Figure 13b** (timepoint as indicated). g, Target engagement in LNCaP cell line using **3** and **ent-3** corresponding to **Supplementary Figure 13c**. h, Selectivity profile against various DUBs in LNCaP cell line

corresponding to **Supplementary Figure 13d**. i, Target engagement using **3** in SJSA-1 cell line corresponding to **Supplementary Figure 14d**.

## SUPPLEMENTARY INFORMATION - Tables

### Supplementary Table 1: Crystallographic data collection and refinement statistics (molecular replacement)

| | USP7/**2**, 5N9R | USP7/**4**, 5N9T |
|---|---|---|
| **Data collection** | | |
| Space group | $P2_1$ | $P2_1$ |
| Cell dimensions | | |
| *a*, *b*, *c* (Å) | 74.94, 66.94, 81.09 | 75.51, 67.62, 81.05 |
| α, β, γ (°) | 90.00, 105.09, 90.00 | 90.00, 105.90, 90.00 |
| Resolution (Å) | 20.00-2.23 (2.29-2.25) | 29.92-1.73 (1.82-1.73) |
| $R_{merge}$ | 0.06 (0.31) | 0.08 (0.65) |
| $I / \sigma I$ | 16.4 (4.5) | 5.7 (1.2) |
| Completeness (%) | 99.2 (99.4) | 94.3 (94.3) |
| Redundancy | 3.5(3.4) | 2.2 (2.2) |
| **Refinement** | | |
| Resolution (Å) | 30.00-2.23 (2.29-2.23) | 29.92-1.73 (1.82-1.73) |
| No. reflections | 35975 (1848) | 73492 (3826) |
| $R_{work}$ / $R_{free}$ | 0.148 / 0.212 | 0.175 / 0.232 |
| No. atoms | | |
| Protein | 5763 | 5813 |
| Ligand/ion | 97 | 115 |
| Water | 528 | 880 |
| *B*-factors | | |
| Protein | 64.54 | 43.62 |
| Ligand/ion | 58.54 | 40.11 |
| Water | 64.08 | 52.40 |
| R.m.s. deviations | | |
| Bond lengths (Å) | 0.009 | 0.011 |
| Bond angles (°) | 1.378 | 1.475 |

* Data were collected from a single crystal for each structure. Values in parentheses are for the highest-resolution shell.

**Supplementary Table 2: F-Test statistical analysis.** See Online Methods section and main text for more details.

| | **Analysis 1** | **Analysis 1** | **Analysis 1** |
|---|---|---|---|
| **Inhibition Mode** | Non-competitive Inhibition | Non-competitive Inhibition | Competitive Inhibition |
| **Number of Parameters** | 3 | 3 | 3 |
| | **Analysis 2** | **Analysis 2** | **Analysis 2** |
| **Inhibition Mode** | Competitive Inhibition | Uncompetitive Inhibition | Uncompetitive Inhibition |
| **Number of Parameters** | **3** | **3** | **3** |
| **Number of data points:** | 76 | 76 | 76 |
| **Chi2 Value (1)** | 572.881 | 572.881 | 3307.05 |
| **Chi2 Value (2)** | 3307.05 | 1352.63 | 1352.63 |
| **F statistic:** | 5.77267 | 2.36111 | 2.4449 |
| **Probability:** | 1.72E-12 | 0.000313566 | 0.00017992 |

**Supplementary Table 3: Anti-proliferative activity of USP7 inhibitors and benchmarking to MDM2 antagonists**

| Cell lines / $EC_{50}$ (nM) | ***3*** | ***nutlin-3a*** | ***RG7112*** | ***SAR405838*** | ***ent-3*** |
|---|---|---|---|---|---|
| **RS4;11** | 2.0±0.9 | 140±38 | 62.0±15.0 | 32.0±10.0 | 2200±730 |
| **LNCaP** | 29.0±4.0 | 620±160 | 170.0±25.0 | 64.0±25 | 9300±2900 |
| **SJSA-1** | >20000 | 960±45 | 320±43 | 100±25 | >20000 |

See Online Methods section and main text for more details. Enantiomer (*ent-*). Data reported is the mean of at least 3 independent experiments ± standard deviations.

1

2

3

4

5

6

7

**SUPPLEMENTARY NOTE – Synthetic Procedures**

Abbreviations and Acronyms

aq: aqueous;; Boc: *tert*-butyloxycarbonyl; DCM: dichloromethane; br: broad; d: doublet; DIPEA: diisopropylethylamine; DME: dimethoxyethane; DMF: *N*,*N*-dimethylformamide; DMSO: dimethylsulfoxide; EDC: *N*-(3-dimethylaminopropyl)-*N*'-ethylcarbodiimide hydrochloride; EtOAc: ethyl acetate; PE: petroleum ether 40/60; ee: enantiomeric excess; ESI: electrospray ionization; h: hour; HATU: *N*-[(dimethylamino)-1*H*-1,2,3-triazolo-[4,5-*b*]pyridin-1-ylmethylene]-*N*-methylmethanaminium hexafluorophosphate *N*-oxide; HPLC: high pressure liquid chromatography; LC: liquid chromatography; LCMS: liquid chromatography mass spectrometry; M: molar; *m/z*: mass-to-charge ratio; MeCN: acetonitrile; MeOH: methanol; min: minutes; MS: mass spectrometry; m: multiplet; NMR: nuclear magnetic resonance; q: quartet; quint: quintet; $R_T$: retention time; RT: room temperature; s: singlet; SPhos: 2-dicyclohexylphosphino-2',6'-dimethoxybiphenyl; TFA: trifluoroacetic acid; THF: tetrahydrofuran; t: triplet; v/v: volume per unit volume; Walphos SL-W008-2:(*S*)-1-{($S_P$)-2-[2-(dicyclohexylphosphino)phenyl]ferrocenyl}ethylbis[3,5-bis(trifluoromethyl)phenyl]phosphine;

General Experimental Conditions

*Solvents and reagents*

Common organic solvents that were used in reactions (e.g. THF, DMF, DCM, and methanol) were purchased anhydrous from Sigma-Aldrich® in Sure/Seal™ bottles and were handled appropriately under nitrogen. Water was deionised using an Elga PURELAB Option-Q. All other solvents used (i.e. for work-up procedures and purification) were generally HPLC grade and were used as supplied from various commercial sources. Unless otherwise stated, all starting materials used were purchased from commercial suppliers and used as supplied.

*Microwave synthesis*

Microwave experiments were carried out using a Biotage Initiator™ Eight system.

*Flash chromatography*

Purification of compounds by flash chromatography was achieved using a Biotage Isolera Four system using the stated cartridges.

*NMR spectroscopy*

$^{1}$H NMR spectra were recorded at ambient temperature using a Bruker Avance (300 MHz), Bruker Avance III (400 MHz) or Bruker Ascend (500 MHz) spectrometer. All chemical shifts (δ) are expressed in ppm. Residual solvent signals were used as an internal standard and the characteristic solvent peaks were corrected to the reference data outlined in *J. Org. Chem.*, 1997, 62, p7512-7515; in other cases, NMR solvents contained tetramethylsilane, which was used as an internal standard.

*Liquid Chromatography Mass Spectrometry (LCMS)*

Liquid Chromatography Mass Spectrometry (LCMS) experiments to determine retention times ($R_T$) and associated mass ions were performed using the following methods:

Method A: The system consisted of an Agilent Technologies 6130 quadrupole mass spectrometer linked to an Agilent Technologies 1290 Infinity LC system with UV diode array detector and autosampler. The spectrometer consisted of an electrospray ionization source operating in positive and negative ion mode. LCMS experiments were performed on each sample submitted using the following conditions: LC Column: Agilent Eclipse Plus C18 RRHD, 1.8 µm, 50 x 2.1 mm maintained at 40 °C. Mobile phases: A) 0.1% (v/v) formic acid in water; B) 0.1% (v/v) formic acid in acetonitrile.

| Gradient Time (min) | Flow (mL/min) | %A | %B |
|---|---|---|---|
| 0.00 | 0.5 | 80 | 20 |
| 1.80 | 0.5 | 0 | 100 |
| 2.20 | 0.5 | 0 | 100 |
| 2.50 | 0.5 | 80 | 20 |
| 3.00 | 0.5 | 80 | 20 |

Method B: The system consisted of an Agilent Technologies 6140 single quadrupole mass spectrometer linked to an Agilent Technologies 1290 Infinity LC system with UV diode array detector and autosampler. The spectrometer consisted of a multimode ionization source (electrospray and atmospheric pressure chemical ionizations)

operating in positive and negative ion mode. LCMS experiments were performed on each sample submitted using the following conditions: LC Column: Zorbax Eclipse Plus C18 RRHD, 1.8 µm, 50 x 2.1 mm maintained at 40 °C. Mobile phases: A) 0.1% (v/v) formic acid in water; B) 0.1% (v/v) formic acid in acetonitrile.

| Gradient Time (min) | Flow (mL/min) | %A | %B |
|---|---|---|---|
| 0.00 | 1.0 | 95 | 5 |
| 1.80 | 1.0 | 0 | 100 |
| 2.20 | 1.0 | 0 | 100 |
| 2.21 | 1.0 | 95 | 5 |
| 2.50 | 1.0 | 95 | 5 |

*Nomenclature*

Unless otherwise indicated, the nomenclature of structures was determined using the 'Convert Structure to Name' function of ChemBioDraw Ultra 12.0.2 (CambridgeSoft/PerkinElmer).

**Compound 1**

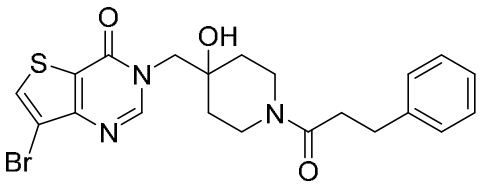


*Step 1: 1-(3-Phenylpropanoyl)piperidin-4-one* (**8**)*::*

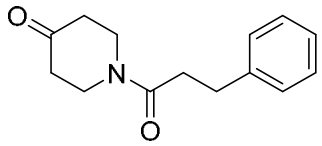

A solution of *tert*-butyl 4-oxopiperidine-1-carboxylate (5 g, 25.1 mmol) in DCM (25 mL) and TFA (9.67 mL, 125 mmol) was stirred at RT for 24 h before the solvent was removed *in vacuo* and the product dried under high vacuum. To a stirred suspension of the TFA salt in dry DCM (125 mL) was added DIPEA (13.2 mL, 75.0 mmol) before 3-phenylpropanoic acid (4.52 g, 30.1 mmol), EDC (6.26 g, 32.6 mmol) and DMAP (0.307 g, 2.51 mmol) were added. The reaction mixture was stirred at RT for 18 h, diluted with DCM (150 mL) and washed with saturated $NaHCO_{3(aq)}$ (250 mL). The aqueous layer was further extracted with DCM (75 mL) before the combined organic phases were washed with 3% $HCl_{(aq)}$ (150 mL) and brine (150 mL). The combined organic phases were passed through a Biotage phase separator, concentrated *in vacuo* and purified by flash chromatography (Biotage KP-Sil 100 g cartridge, 0-100% EtOAc in PE) to give the title compound as pale yellow oil. LCMS (Method A): $R_T$ = 0.89 min, *m/z* = 232 $[M+H]^+$. $^1$H NMR (300 MHz, $CDCl_3$): δ 7.37 – 7.15 (m, 5H), 3.89 (t, *J* = 6.4 Hz, 2H), 3.66 (t, *J* = 6.3 Hz, 2H), 3.04 (dd, *J* = 8.5, 6.8 Hz, 2H), 2.73 (dd, *J* = 8.4, 6.9 Hz, 2H), 2.44 (t, *J* = 6.4 Hz, 2H), 2.26 (t, *J* = 6.3 Hz, 2H). $^{13}$C NMR (75 MHz, $CDCl_3$): δ 206.87, 171.14, 141.06, 128.71, 128.59, 126.51, 44.24, 41.15, 40.94, 40.92, 35.01, 31.70.

*Step 2: 3-Phenyl-1-(1-oxa-6-azaspiro[2.5]octan-6-yl)propan-1-one* (**9**)*:*

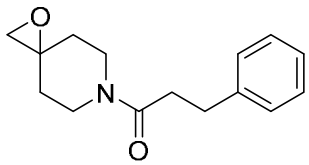

To a solution of trimethylsulfonium iodide (4.59 g, 22.5 mmol) in dry DMSO (20 mL) was added a 60% dispersion of NaH in mineral oil (0.899 g, 22.5 mmol). The resulting mixture was stirred at RT for 1 h before a solution of 1-(3-phenylpropanoyl)piperidin-4-one (2.08 g, 8.99 mmol) in dry DMSO (10 mL) was added. The reaction mixture was stirred at 50 °C for 2 h before it was allowed to cool to RT and quenched by the addition of water (100 mL). The resulting mixture was extracted with $Et_2O$ (3 x 50 mL), the combined organic extracts were washed with brine, dried over $Na_2SO_4$, concentrated *in vacuo*, and the product was purified by flash chromatography (Biotage KP-Sil 50 g cartridge, 0-60% EtOAc in PE) to give the title compound (1.41 g, 64%) as a colourless oil. LCMS (Method A): $R_T$ = 1.07 min, *m/z* = 246 $[M+H]^+$. $^1$H NMR (300 MHz, $CDCl_3$): δ 7.38 – 7.09 (m, 5H), 4.21 – 4.05 (m, 1H), 3.70 – 3.53 (m, 1H), 3.42 (tdd, *J* = 13.5, 10.0, 3.6 Hz, 2H), 3.08 – 2.89 (m, 2H), 2.77 – 2.55 (m, 4H), 1.81 (ddd, *J* = 14.2, 10.0, 4.5 Hz, 1H), 1.68 (ddd, *J* = 13.7, 8.1, 4.5 Hz, 1H), 1.49 – 1.29 (m, 2H). $^{13}$C NMR (75 MHz, $CDCl_3$): δ 170.77, 141.37, 128.65, 128.58, 126.34, 57.04, 53.84, 44.29, 40.55, 35.23, 33.64, 32.79, 31.73.

*Step 3: 7-Bromo-3-((4-hydroxy-1-(3-phenylpropanoyl)piperidin-4-yl)methyl)thieno[3,2-d]pyrimidin-4(3H)-one* (**1**)*:*

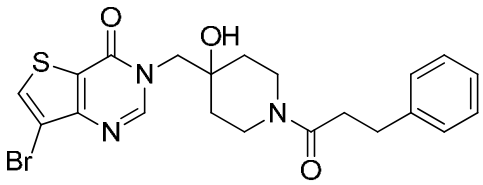


A mixture of 3-phenyl-1-(1-oxa-6-azaspiro[2.5]octan-6-yl)propan-1-one (206 mg, 0.840 mmol), 7-bromothieno[3,2-*d*]pyrimidin-4(3*H*)-one[1] (176 mg, 0.763 mmol) and $Cs_2CO_3$ (298 mg, 0.916 mmol) in DMF (8 mL) was heated at 80 °C for 16 h. Upon cooling

to RT, the mixture was diluted with saturated $NH_4Cl_{(aq)}$ (40 mL) and extracted with DCM (3 x 30 mL) using a Biotage phase separator. The combined organic phases were concentrated *in vacuo* and the residue was purified by flash chromatography (Biotage KP-NH 11 g cartridge, 0-30% MeOH in DCM) to give the title compound (204 mg, 56%) as a colourless solid. LCMS (Method A): $R_T$ = 1.22 min (purity >98% at 254 nm), *m/z* = 476, 478 $[M+H]^+$. $^1H$ NMR (500 MHz, DMSO-$d_6$): δ 8.39 (s, 2H), 7.33 – 7.10 (m, 5H), 4.96 (s, 1H), 4.11 – 4.06 (m, 1H), 4.06 – 3.96 (m, 2H), 3.67 – 3.59 (m, 1H), 3.25 – 3.16 (m, 1H), 2.93 – 2.85 (m, 1H), 2.80 (t, *J* = 7.7 Hz, 2H), 2.67 – 2.53 (m, 2H), 1.49 – 1.32 (m, 4H). $^{13}C$ NMR (126 MHz, DMSO-$d_6$): δ 169.58, 156.66, 153.40, 151.22, 141.44, 132.49, 128.37, 128.17, 125.78, 121.88, 108.30, 69.21, 53.64, 40.78, 36.92, 34.82, 34.14, 33.86, 30.87. HRMS (TOF MS ES+): *m/z* $[M + H]^+$ Calcd for $C_{21}H_{23}N_3O_3SBr$ 476.0644, found 476.0642.

**Compound 2**

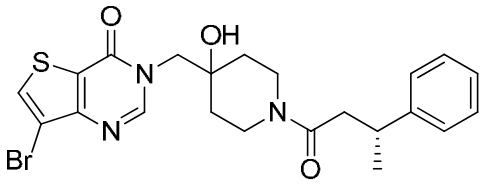


*Step 1: tert-Butyl 4-((7-bromo-4-oxothieno[3,2-d]pyrimidin-3(4H)-yl)methyl)-4-hydroxypiperidine-1-carboxylate* (**10**)*::*

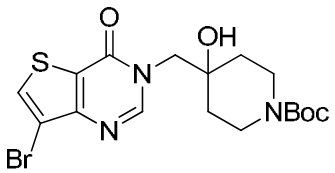

A mixture of *tert*-butyl 1-oxa-6-azaspiro[2.5]octane-6-carboxylate (640 mg, 3.00 mmol), 7-bromothieno[3,2-*d*]pyrimidin-4(3*H*)-one[1] (578 mg, 2.50 mmol) and $Cs_2CO_3$ (978 mg, 3.00 mmol) in DMF (8.3 mL) was heated at 80 °C for 16 h. Upon cooling to RT, the mixture was diluted with saturated $NH_4Cl_{(aq)}$ (40 mL) and extracted with DCM (3 x 30 mL) using a Biotage phase separator. The combined organic phases were concentrated *in vacuo* and the residue was purified by flash chromatography (GraceResolv silica 80 g cartridge, 0-100% EtOAc in cyclohexane) to give the title compound (867 mg, 78%) as a pale yellow solid. LCMS (Method A): $R_T$ = 1.31 min, *m/z* = 466, 468 $[M+Na]^+$. $^1$H NMR (300 MHz, DMSO-$d_6$): δ 8.40 (s, 2H), 4.95 (s, 1H), 4.11 – 3.95 (m, 2H), 3.76 – 3.54 (m, 2H), 3.14 – 2.91 (m, 2H), 1.57 – 1.27 (m, 4H), 1.39 (s, 9H). $^{13}$C NMR (75 MHz, $CDCl_3$): δ 157.99, 154.72, 154.01, 149.91, 131.82, 122.92, 109.26, 79.80, 70.44, 55.50, 39.46, 34.98, 28.48.

*Step 2: 7-Bromo-3-((4-hydroxypiperidin-4-yl)methyl)thieno[3,2-d]pyrimidin-4(3H)-one* (**11**)*:*

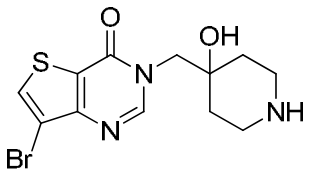


A solution of *tert*-butyl 4-((7-bromo-4-oxothieno[3,2-*d*]pyrimidin-3(4*H*)-yl)methyl)-4-hydroxypiperidine-1-carboxylate (250 mg, 0.563 mmol) was stirred in DCM (3 mL) and TFA (3 mL) for 20 min before the reaction was purified using a 10 g SCX-2 cartridge (10% MeOH in DCM then 20% 7 M $NH_3$ in MeOH in DCM) to give the title compound (189 mg, 98%) as a colourless solid. LCMS (Method A): $R_T$ = 0.36 min, *m/z* = 344, 346 $[M+H]^+$. $^1$H NMR (400 MHz, $CDCl_3$): δ 8.30 (s, 1H), 7.78 (s, 1H), 4.11 (s, 2H), 2.95 – 2.85

(m, 4H), 1.70 – 1.58 (m, 2H), 1.56 – 1.46 (m, 2H). $^{13}$C NMR (101 MHz, $CDCl_3$): δ 158.07, 154.07, 150.04, 131.75, 123.03, 109.35, 70.63, 55.50, 42.03, 36.30.

*Step 3: (R)-7-Bromo-3-((4-hydroxy-1-(3-phenylbutanoyl)piperidin-4-yl)methyl)thieno[3,2-d]pyrimidin-4(3H)-one* (**2**)*:*

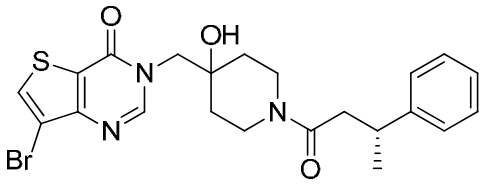


DIPEA (0.359 mL, 2.06 mmol) was added to a suspension of 7-bromo-3-((4-hydroxypiperidin-4-yl)methyl)thieno[3,2-*d*]pyrimidin-4(3*H*)-one (177 mg, 0.514 mmol), (*R*)-3-phenylbutanoic acid (101 mg, 0.617 mmol) and HATU (235 mg, 0.617 mmol) in DCM (10.3 mL). After 10 min, the reaction was quenched by the addition of saturated $NaHCO_{3(aq)}$ (30 mL) and the mixture was extracted with DCM (3 x 40 mL) using a Biotage phase separator. The combined organic phases were concentrated *in vacuo* and the residue was purified by flash chromatography (GraceResolv silica 40 g cartridge, 0-100% EtOAc in cyclohexane then 0-30% MeOH in EtOAc) to give the title compound (134 mg, 53%) as a colourless solid. LCMS (Method A): $R_T$ = 1.28 min (purity >95% at 254 nm), *m/z* = 490, 492 $[M+H]^+$. $^1$H NMR (500 MHz, DMSO-$d_6$): δ 8.57 – 8.16 (m, 2H), 7.46 – 7.03 (m, 5H), 5.00 – 4.88 (m, 1H), 4.13 – 3.87 (m, 3H), 3.71 – 3.58 (m, 1H), 3.25 – 3.08 (m, 2H), 2.91 – 2.77 (m, 1H), 2.66 – 2.52 (m, 2H), 1.58 – 1.13 (m, 7H). $^{13}$C NMR (126 MHz, DMSO-$d_6$): δ 169.08 + 169.06 (conformers), 156.67 + 156.62 (conformers), 153.38, 151.23 + 151.20 (conformers), 146.66 + 146.54 (conformers), 132.49, 128.18 + 128.15 (conformers), 126.88 + 126.85 (conformers), 125.93 + 125.89

(conformers), 121.87, 108.30, 69.20 + 69.15 (conformers), 53.61, 41.01 + 40.90 (conformers), 40.22 + 40.19 (conformers), 36.87, 36.21 + 35.99 (conformers), 34.93 + 34.80 (conformers), 34.25 + 34.12 (conformers), 22.06 + 21.86 (conformers). HRMS (TOF MS ES+): *m/z* $[M + H]^+$ Calcd for $C_{22}H_{25}N_3O_3SBr$ 490.0800, found 490.0793.

**Compound 5 *(ent*-2*)***

Compound *ent*-2 was made by an identical method as **2** starting from *7-Bromo-3-((4-hydroxypiperidin-4-yl)methyl)thieno[3,2-d]pyrimidin-4(3H)-one* but using (*S*)-3-phenylbutanoic acid in the coupling step.

**Compound 3**

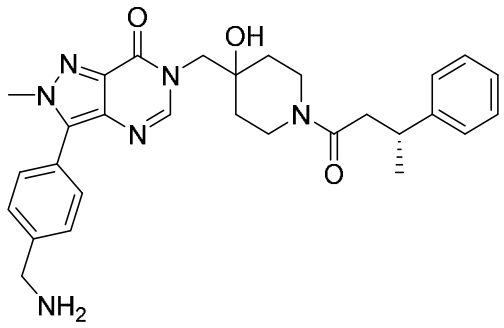

*Step 1: 3-Bromo-2-methyl-2H-pyrazolo[4,3-d]pyrimidin-7(6H)-one* (**12**)*:*

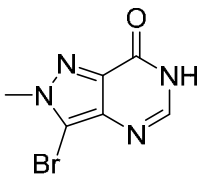

Bromine (3.34 mL, 64.7 mmol) was added to a suspension of 2-methyl-2*H*-pyrazolo[4,3-*d*]pyrimidin-7(6*H*)-one[2] (3.24 g, 21.6 mmol) in AcOH (21.6 mL) in a reaction tube. The tube was sealed and the mixture was heated at 95 °C for 18 h

before being cooled to RT and 1:1 EtOH/$Et_2O$ (100 mL) was added. Saturated sodium thiosulfate$_{(aq)}$ (50 mL) was added and once the colour had dissipated, the product was isolated by filtration. The resulting precipitate was washed with water (3 x 50 mL) and dried under high vacuum at 75 °C to give the title compound (4.80 g, 97%) as a pale yellow solid. LCMS (Method A): $R_T$ = 0.40 min, *m/z* = 229, 231 $[M+H]^+$. $^1$H NMR (500 MHz, DMSO-$d_6$): δ 12.02 (br. s, 1H), 7.84 (d, *J* = 3.5 Hz, 1H), 4.07 (s, 3H). $^{13}$C NMR (126 MHz, DMSO-$d_6$): δ 155.79, 144.12, 136.49, 135.77, 109.04, 39.26.

*Step 2: tert-Butyl 4-((3-bromo-2-methyl-7-oxo-2H-pyrazolo[4,3-d]pyrimidin-6(7H)-yl)methyl)-4-hydroxypiperidine-1-carboxylate* (**13**)*:*

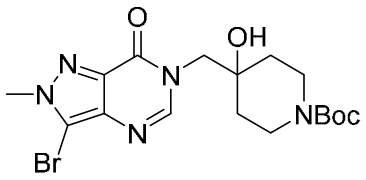


A suspension of *tert*-butyl 1-oxa-6-azaspiro[2.5]octane-6-carboxylate (5.59 g, 26.2 mmol) , 3-bromo-2-methyl-2*H*-pyrazolo[4,3-*d*]pyrimidin-7(6*H*)-one (3 g, 13.1 mmol) and $Cs_2CO_3$ (4.69 g, 14.4 mmol) in DMF (44 mL) was heated at 80 °C for 18 h. Upon cooling to RT, the reaction was quenched by the addition of saturated $NH_4Cl_{(aq)}$ (200 mL) and the mixture was extracted with EtOAc (3 x 50 mL). The combined organic phases were passed through a Biotage phase separator, concentrated *in vacuo* and the residue was purified by flash chromatography (GraceResolv silica 220 g cartridge, 0-100% EtOAc in cyclohexane then 0-15% MeOH in EtOAc) to give the title compound (4.22 g, 73%) as a pale yellow foam. LCMS (Method A): $R_T$ = 1.06 min, *m/z* = 464, 466 $[M+Na]^+$. $^1$H NMR (500 MHz, $CDCl_3$): δ 7.93 (s, 1H), 4.18 – 3.98 (m, 2H), 4.12 (s, 3H), 3.95 – 3.75 (m, 2H), 3.22 – 3.05 (m, 2H), 1.68 – 1.48 (m, 4H), 1.43 (s, 9H).

$^{13}$C NMR (126 MHz, $CDCl_3$): δ 157.49, 154.78, 147.18, 136.10, 135.65, 109.25, 79.78, 70.73, 55.36, 39.63, 39.38, 35.13, 28.55.

*Step 3: 3-Bromo-6-((4-hydroxypiperidin-4-yl)methyl)-2-methyl-2H-pyrazolo[4,3-d]pyrimidin-7(6H)-one* (**14**)*:*

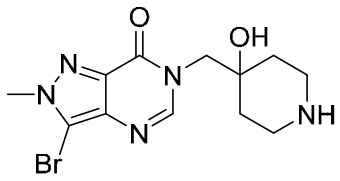


A solution of *tert*-butyl 4-((3-bromo-2-methyl-7-oxo-2*H*-pyrazolo[4,3-*d*]pyrimidin-6(7*H*)-yl)methyl)-4-hydroxypiperidine-1-carboxylate (10 g, 22.6 mmol) in DCM (75 mL) and TFA (37.5 mL) was stirred for 5 min before the reaction mixture was purified using 2 x 70 g SCX-2 cartridges (1:1 DCM/MeOH then 1:1 DCM/7 M in $NH_3$ in MeOH) to give the title compound (7.69 g, 99%) as a colourless foam. LCMS (Method A): $R_T$ = 0.238 min, *m/z* = 342, 344 $[M+H]^+$. $^1$H NMR (500 MHz, DMSO-$d_6$): δ 8.06 (s, 1H), 4.87 (s, 1H), 4.08 (s, 3H), 3.96 (s, 2H), 2.78 (dd, *J* = 8.1, 3.6 Hz, 4H), 1.51 (dt, *J* = 14.7, 7.6 Hz, 2H), 1.36 (dt, *J* = 13.0, 3.8 Hz, 2H). $^{13}$C NMR (126 MHz, DMSO-$d_6$): δ 165.96, 155.76, 148.16, 135.65, 135.02, 108.82, 68.91, 53.16, 40.64, 34.23.

*Step 4: (R)-3-Bromo-6-((4-hydroxy-1-(3-phenylbutanoyl)piperidin-4-yl)methyl)-2-methyl-2H-pyrazolo[4,3-d]pyrimidin-7(6H)-one* (**15**)*:*

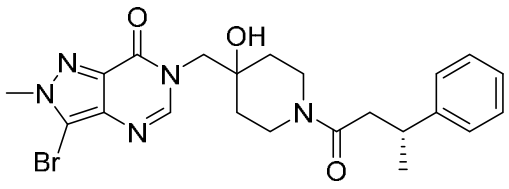

Using a pressure equalized dropping funnel, DIPEA (40.8 mL, 234 mmol) was added dropwise over 35 min to a solution of 3-bromo-6-((4-hydroxypiperidin-4-yl)methyl)-2-methyl-2*H*-pyrazolo[4,3-*d*]pyrimidin-7(6*H*)-one (20 g, 58.4 mmol), (*R*)-3-phenylbutanoic acid (10.6 g, 64.3 mmol) and HATU (24.5 g, 64.3 mmol) in DCM (784 mL). After 2 h, the reaction was quenched by the addition of saturated $NaHCO_{3(aq)}$ (1 L) and the mixture was extracted with DCM (3 x 100 mL). The combined organic phases were passed through a Biotage phase separator, concentrated *in vacuo* and the residue was purified by flash chromatography (Biotage KP-Sil 340 g cartridge, 0-100% EtOAc in cyclohexane then 0-30% MeOH in EtOAc) to give the title compound (26.8 g, 94%) as colourless solid. LCMS (Method A): $R_T$ = 1.06 min, *m/z* = 488, 490 $[M+H]^+$. $^1$H NMR (500 MHz, DMSO-$d_6$): δ 8.07 – 7.97 (m, 1H), 7.34 – 7.08 (m, 5H), 4.90 – 4.80 (m, 1H), 4.08 (s, 3H), 4.08 – 3.84 (m, 3H), 3.69 – 3.58 (m, 1H), 3.26 – 3.10 (m, 2H), 2.91 – 2.81 (m, 1H), 2.65 – 2.52 (m, 2H), 1.54 – 1.22 (m, 4H), 1.20 (d, *J* = 7.0 Hz, 3H). $^{13}$C NMR (126 MHz, DMSO-$d_6$): δ 169.07 + 169.05 (conformers), 155.78 + 155.73 (conformers), 148.07, 146.67 + 146.54 (conformers), 135.65, 135.04, 128.19 + 128.15 (conformers), 126.86 + 126.85 (conformers), 125.95 + 125.88 (conformers), 108.84, 69.28 + 69.23 (conformers), 53.10, 41.03 + 40.91 (conformers), 40.22, 39.31, 36.88, 36.20 + 35.97 (conformers), 34.96 + 34.83 (conformers), 34.21 + 34.09 (conformers), 22.05 + 21.86 (conformers).

*Steps 5 and 6: (R)-3-(4-(Aminomethyl)phenyl)-6-((4-hydroxy-1-(3-phenylbutanoyl)piperidin-4-yl)methyl)-2-methyl-2H-pyrazolo[4,3-d]pyrimidin-7(6H)-one* (**3**)*:*

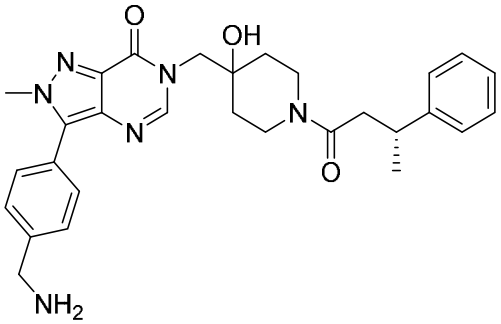


A 1 L round bottom flask was charged with (*R*)-3-bromo-6-((4-hydroxy-1-(3-phenylbutanoyl)piperidin-4-yl)methyl)-2-methyl-2*H*-pyrazolo[4,3-*d*]pyrimidin-7(6*H*)-one (15.6 g, 31.9 mmol), SPhos (786 mg, 1.92 mmol), $Pd(OAc)_2$ (215 mg, 0.958 mmol), (4-(((*tert*-butoxycarbonyl)amino)methyl)phenyl)boronic acid (12.0 g, 47.9 mmol) and $K_3PO_4$ (13.6 g, 63.8 mmol) and was degassed by evacuating and refilling the flask with $N_2$ three times using a Schlenk manifold. Under a $N_2$ atmosphere, *n*-butanol (128 mL) was added before the flask was evacuated and refilled with $N_2$ three times using a Schlenk manifold. The reaction mixture was heated at 100 °C for 2 h before being cooled to RT and concentrated *in vacuo*. The residue was partitioned between water (350 mL) and EtOAc (250 mL). The phases were separated and the aqueous phase was extracted using EtOAc (2 x 50 mL). The combined organic phases were dried over $Na_2SO_4$, concentrated *in vacuo* and the residue was purified by flash chromatography (Biotage KP-Sil 340 g cartridge, 0-100% EtOAc in cyclohexane then 0-20% MeOH in EtOAc), the impure fractions were re-purified using a GraceResolv silica 80 g cartridge, 0-100% EtOAc in cyclohexane then 0-20% MeOH in EtOAc) to give (*R*)-*tert*-butyl 4-(6-((4-hydroxy-1-(3-phenylbutanoyl)piperidin-4-yl)methyl)-2-methyl-7-oxo-6,7-dihydro-2*H*-pyrazolo[4,3-*d*]pyrimidin-3-yl)benzylcarbamate (15.4 g, 78%) as a colourless foam. LCMS (Method A): $R_T$ = 1.37 min, *m/z* = 615 $[M+H]^+$. A solution of (*R*)-*tert*-butyl 4-(6-((4-hydroxy-1-

(3-phenylbutanoyl)piperidin-4-yl)methyl)-2-methyl-7-oxo-6,7-dihydro-2*H*-pyrazolo[4,3-*d*]pyrimidin-3-yl)benzylcarbamate (8.73 g, 14.2 mmol) in DCM (14 mL) and TFA (14 mL) was stirred for 90 min before the reaction was purified using 4 x 10 g SCX-2 cartridges in parallel (1:10 MeOH in DCM then 1:3 7 M in $NH_3$ in MeOH in DCM). The basic phases were combined and concentrated to give the crude product (4.89 g). The DCM/MeOH phases were concentrated and the residue was purified using 4 x 10 g SCX-2 cartridges in parallel (1:10 MeOH in DCM then 1:3 7 M in $NH_3$ in MeOH in DCM) and the basic phases were combined and concentrated to give the crude product (2.62 g). The combined crude products (7.51 g) were purified by flash chromatography (GraceResolve silica 120 g cartridge, 0-30% dilute $NH_3$ in MeOH in DCM) to give the title compound (6.9 g, 94%) as a colourless solid after freeze drying. LCMS (Method A): $R_T$ = 0.71 min (purity >99% at 254 nm), *m/z* = 515 $[M+H]^+$. $^1$H NMR (500 MHz, DMSO-$d_6$): δ 8.03 – 7.92 (m, 1H), 7.69 – 7.43 (m, 4H), 7.30 – 7.21 (m, 4H), 7.19 – 7.12 (m, 1H), 4.87 (s, 1H), 4.10 (s, 3H), 4.07 – 3.86 (m, 3H), 3.81 (s, 2H), 3.70 – 3.61 (m, 1H), 3.28 – 3.12 (m, 2H), 2.93 – 2.83 (m, 1H), 2.66 – 2.52 (m, 2H), 2.31 (br. s, 2H), 1.57 – 1.23 (m, 4H), 1.21 (d, *J* = 6.9 Hz, 3H). $^{13}$C NMR (126 MHz, DMSO-$d_6$): δ 169.07 + 169.05 (conformers), 156.24 + 156.19 (conformers), 147.27, 146.68, 146.56, 145.04, 136.00, 134.59 + 134.41 (conformers), 129.20, 128.20 + 128.16 (conformers), 127.37, 126.86, 125.95 + 125.89 (conformers), 125.31, 69.35 + 69.30 (conformers), 52.94, 45.29, 41.07 + 40.96 (conformers), 40.25 + 40.23 (conformers), 39.51, 36.92, 36.20 + 35.99 (conformers), 35.02 + 34.91 (conformers), 34.27 + 34.14 (conformers), 22.06 + 21.88 (conformers). HRMS (TOF MS ES+): *m/*z $[M + H]^+$ Calcd for $C_{29}H_{35}N_6O_3$ 515.2771, found 515.2773.

**Compound 6 *(ent*-3*)***

Compound *ent*-3 was made by an identical method as **3** starting from *3-Bromo-6-((4-hydroxypiperidin-4-yl)methyl)-2-methyl-2H-pyrazolo[4,3-d]pyrimidin-7(6H)-one* but using (*S*)-3-phenylbutanoic acid in the coupling step.

**Compound 4**

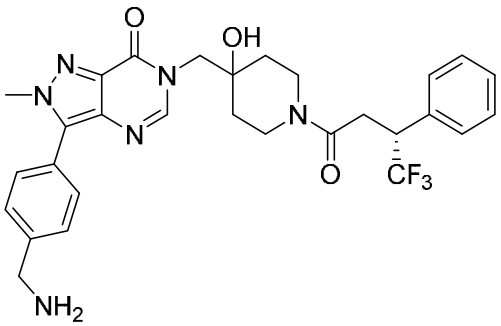


*Step 1: (E)-4,4,4-Trifluoro-3-phenylbut-2-enoic acid* (**16**)*:*

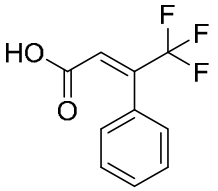


LiOH (132 mg, 5.5 mmol) was added to solution of (*E*)-ethyl 4,4,4-trifluoro-3-phenylbut-2-enoate (*J. Fluorine Chem.* 2013, *152*, 56) (1.22 g, 5 mmol) in THF (10 mL) and water (5 mL) at RT. After 1 h, the pH of the reaction mixture was adjusted to pH 4 by the addition of 1 M $HCl_{(aq)}$ and the mixture was extracted with DCM (3 x 10 mL) using a Biotage phase separator. The combined organic phases were concentrated and the product was dried *in vacuo* to give (*E*)-4,4,4-trifluoro-3-phenylbut-2-enoic acid (1.06 g, 98%) as a colourless solid. LCMS (Method A): $R_T$ = 1.27 min, *m/z* = 215 $[M-H]^-$. $^1H$ NMR (400 MHz, DMSO-$d_6$): δ 13.21 (s, 1H), 7.48 – 7.39 (m, 3H), 7.31 (dd, *J*

= 6.6, 2.9 Hz, 2H), 6.84 (q, *J* = 1.5 Hz, 1H). $^{19}$F NMR (376 MHz, DMSO-$d_6$): δ -65.64. $^{13}$C NMR (101 MHz, DMSO-$d_6$): δ 165.33, 137.24 (q, *J* = 30.0 Hz), 130.70, 129.33, 128.59, 128.41, 127.63 (q, *J* = 5.4 Hz), 122.87 (q, *J* = 274.5 Hz).

*Step 2: (R)-4,4,4-Trifluoro-3-phenylbutanoic acid* (**17**)*:*

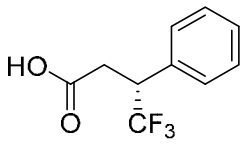


A suspension of *bis*(norbornadiene)rhodium(I) tetrafluoroborate (30.5 mg, 81.8 µmol) and Walphos SL-W008-2 (77 mg, 81.8 µmol) in MeOH (100 mL) in a 300 mL glass reactor autoclave was degassed with $N_2$. After 30 min, a solution was obtained and (*E*)-4,4,4-trifluoro-3-phenylbut-2-enoic acid (900 mg, 4.16 mmol) was added. The reaction was stirred under 5.8 bar $H_2$ for 24 h before being concentrated *in vacuo* to give the title compound (1 g, >100%) as a colourless solid. This material was used without further purification. LCMS (Method A): $R_T$ = 1.24 min, *m/z* = 217 $[M-H]^-$. $^1$H NMR (500 MHz, $CDCl_3$): δ 7.40 – 7.28 (m, 5H), 3.87 (pd, *J* = 9.3, 4.9 Hz, 1H), 3.07 (dd, *J* = 16.8, 4.9 Hz, 1H), 2.93 (dd, *J* = 16.8, 9.7 Hz, 1H). Spectral data matches that reported in the literature.[3]

A 2 M TMS-diazomethane solution in hexanes (0.110 mL, 0.220 mmol) was added to a solution of (*R*)-4,4,4-trifluoro-3-phenylbutanoic acid (24 mg, 0.110 mmol) in MeOH (20 µL) and toluene (0.2 mL). After 1 hour, the reaction mixture was purified directly by chromatography (10 x 0.75 cm silica plug, 0-30% $Et_2O$ in pentane) to give (*R*)-methyl 4,4,4-trifluoro-3-phenylbutanoate (22 mg, 86%) as a pale yellow oil. The $Et_2O$/pentane were removed carefully to avoid loss of material.

The *ee* was measured using a Diacel OJ-H column (250 x 4.6 mm, 5 micron) and 1% *i*PrOH in hexane as the mobile phase. The racemic sample gave 2 peaks: $R_T$ = 23.220 min (49.9021%) and $R_T$ = 26.365 min (50.0979%). This sample gave the same 2 peaks: $R_T$ = 23.401 min (0.6863%) and $R_T$ = 26.099 min (99.3137%). This corresponds to an *ee* measurement for the acid that is >98%. The acid was assigned as *R* by comparison with literature[3] in which the authors use the same OJ stationary phase under which conditions the (*R*)-enantiomer has the longer retention time.

*Step 3: (R)-3-Bromo-6-((4-hydroxy-1-(4,4,4-trifluoro-3-phenylbutanoyl)piperidin-4-yl)methyl)-2-methyl-2H-pyrazolo[4,3-d]pyrimidin-7(6H)-one* (**18**)*:*

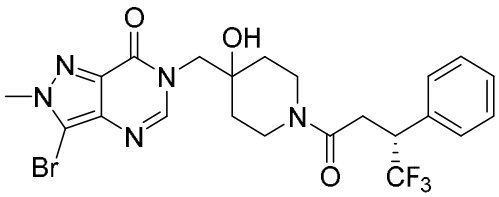


DIPEA (0.224 mL, 1.28 mmol) was added to a suspension of 3-bromo-6-((4-hydroxypiperidin-4-yl)methyl)-2-methyl-2*H*-pyrazolo[4,3-*d*]pyrimidin-7(6*H*)-one (132 mg, 0.385 mmol), (*R*)-4,4,4-trifluoro-3-phenylbutanoic acid (70 mg, 0.32 mmol) and HATU (122 mg, 0.32 mmol) in DCM (20 mL). After 16 h, the reaction was quenched by the addition of saturated $NaHCO_{3(aq)}$ (20 mL) and the mixture was extracted with DCM (3 x 20 mL) using a Biotage phase separator. The combined organic phases were concentrated *in vacuo* and the residue was purified by flash chromatography (Biotage KP-NH 11 g cartridge, 0-100% EtOAc in cyclohexane then 0-30% MeOH in EtOAc) to give the title compound (142 mg, 82%) as a colourless solid. LCMS (Method B): $R_T$ = 1.19 min, *m/z* 542, 544 $[M+H]^+$. $^1$H NMR (500 MHz, DMSO-$d_6$): δ 8.07 – 7.97 (m, 1H), 7.49 – 7.20 (m, 5H), 4.88 (s, 1H), 4.15 – 4.04 (m, 1H), 4.08 (s, 3H),

4.00 – 3.83 (m, 3H), 3.80 – 3.71 (m, 1H), 3.29 – 3.11 (m, 2H), 3.00 – 2.77 (m, 2H), 1.64 – 1.12 (m, 4H). $^{13}$C NMR (126 MHz, DMSO-$d_6$): δ 166.60 + 166.50 (conformers), 155.78 + 155.72 (conformers), 148.08 + 148.06 (conformers), 135.66, 135.05 + 135.03 (conformers), 134.81 – 134.60 (m, due to conformers and coupling with $CF_3$), 129.16, 128.37 + 128.34 (conformers), 128.02 + 127.98 (conformers), 108.86, 69.25 + 69.15 (conformers), 53.15 + 53.06 (conformers), 45.65 – 44.83 (m, due to conformers and coupling with $CF_3$), 40.79, 37.33 + 37.24 (conformers), 34.82 + 34.76 (conformers), 34.05 + 33.99 (conformers), 31.44. Signal for N*C*H$_3$ is under DMSO and the $CF_3$ is not observed.

*Steps 4 and 5: (R)-3-(4-(Aminomethyl)phenyl)-6-((4-hydroxy-1-(4,4,4-trifluoro-3-phenylbutanoyl)piperidin-4-yl)methyl)-2-methyl-2H-pyrazolo[4,3-d]pyrimidin-7(6H)-one* (**4**)*:*

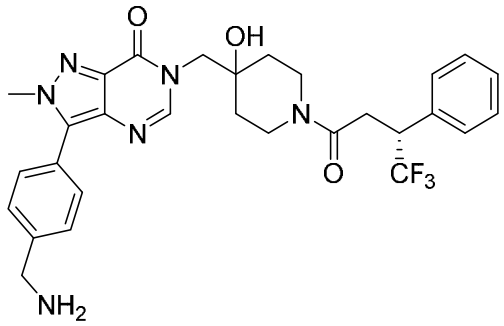


A mixture of (*R*)-3-bromo-6-((4-hydroxy-1-(4,4,4-trifluoro-3-phenylbutanoyl)piperidin-4-yl)methyl)-2-methyl-2*H*-pyrazolo[4,3-*d*]pyrimidin-7(6*H*)-one (250 mg, 0.461 mmol) , (4-(((*tert*-butoxycarbonyl)amino)methyl)phenyl)boronic acid (231 mg, 0.922 mmol), $Pd(PPh_3)_4$ (53 mg, 0.046 mmol), $K_3PO_4$ (391 mg, 1.84 mmol), 1,4-dioxane (3 mL) and water (1 mL) in a reaction tube was degassed by bubbling $N_2$ for 20 min. The reaction tube was sealed and the reaction was heated at

130 °C under microwave irradiation for 30 min. The reaction mixture was diluted with saturated $NH_4Cl_{(aq)}$ (40 mL) and extracted with DCM (3 x 30 mL) using a Biotage phase separator. The combined organic phases were concentrated *in vacuo* and the residue was purified by flash chromatography (40 g GraceResolv silica, 0-100% EtOAc in cyclohexane then 0-10% MeOH in EtOAc) to give (*R*)-*tert*-butyl 4-(6-((4-hydroxy-1-(4,4,4-trifluoro-3-phenylbutanoyl)piperidin-4-yl)methyl)-2-methyl-7-oxo-6,7-dihydro-2*H*-pyrazolo[4,3-*d*]pyrimidin-3-yl)benzylcarbamate (200 mg, 65%) as a pale yellow solid. LCMS (Method A): $R_T$ = 1.47 min, *m/z* 669 $[M+H]^+$.

A solution of (*R*)-*tert*-butyl 4-(6-((4-hydroxy-1-(4,4,4-trifluoro-3-phenylbutanoyl)piperidin-4-yl)methyl)-2-methyl-7-oxo-6,7-dihydro-2*H*-pyrazolo[4,3-*d*]pyrimidin-3-yl)benzylcarbamate (200 mg, 0.300 mmol) in DCM (2 mL) and TFA (1 mL) was stirred at RT for 15 min. The reaction mixture was purified using a 10 g SCX-2 cartridge (MeOH then 7 M in $NH_3$ in MeOH). The basic phases were combined, concentrated *in vacuo* and the residue was purified by flash chromatography (GraceResolv silica 24 g cartridge, 0-100%, EtOAc in cyclohexane then 0-25% MeOH in EtOAc; then Biotage KP-NH 11 g cartridge, 0-100%, EtOAc in cyclohexane then 0-10% MeOH in EtOAc) to give the title compound (90 mg, 52%) as a colourless solid after lyophilization. LCMS (Method B): $R_T$ = 0.81 min (purity >99% at 254 nm), *m/z* 569 $[M+H]^+$. $^1$H NMR (500 MHz, DMSO-$d_6$): δ 8.02 – 7.93 (m, 1H), 7.70 – 7.60 (m, 2H), 7.57 – 7.44 (m, 2H), 7.43 – 7.38 (m, 2H), 7.38 – 7.28 (m, 3H), 4.88 (s, 1H), 4.26 – 4.02 (m, 1H), 4.10 (s, 3H), 4.02 – 3.85 (m, 3H), 3.81 (s, 2H), 3.80 – 3.71 (m, 1H), 3.26 – 3.11 (m, 2H), 3.02 – 2.80 (m, 2H), 2.43 (s, 2H), 1.61 (td, J = 12.7, 12.1, 4.3 Hz, 0.5H), 1.44 – 1.32 (m, 2.5H), 1.27 – 1.17 (m, 1H). $^{13}$C NMR (126 MHz, DMSO-$d_6$): δ 166.60 + 166.50 (conformers), 156.24 + 156.18 (conformers), 147.27 + 147.25 (conformers), 145.22,

136.02, 134.85 – 134.24 (m, due to conformers and coupling with $CF_3$), 129.19, 129.16, 128.37, 128.34, 128.28, 128.22, 128.02, 127.99, 127.34, 127.23, 126.07, 126.04, 125.26, 69.30 + 69.21 (conformers), 52.98 + 52.89 (conformers), 45.46 – 44.90 (m, due to conformers and coupling with $CF_3$), 45.35, 40.83, 39.39, 37.36 + 37.28 (conformers), 34.89 + 34.80 (conformers), 34.09 + 34.04 (conformers), 31.44. The signals between 130 – 125 ppm are complex due to the conformers and the $CF_3$ signals. HRMS (TOF MS ES+): *m/*z $[M + H]^+$ Calcd for $C_{29}H_{32}N_6O_3F_3$ 569.2488, found 569.2509.

**References**

1 Bae, I. H. *et al.* PCT Int. Appl. (2013), WO 2013100632.

2 Oslob, J. D. *et al.* PCT Int. Appl. (2007), WO 2007013964.

3 Dong K. *et al. Angew. Chem. Int. Ed.* **2013**, *52*, 14191.

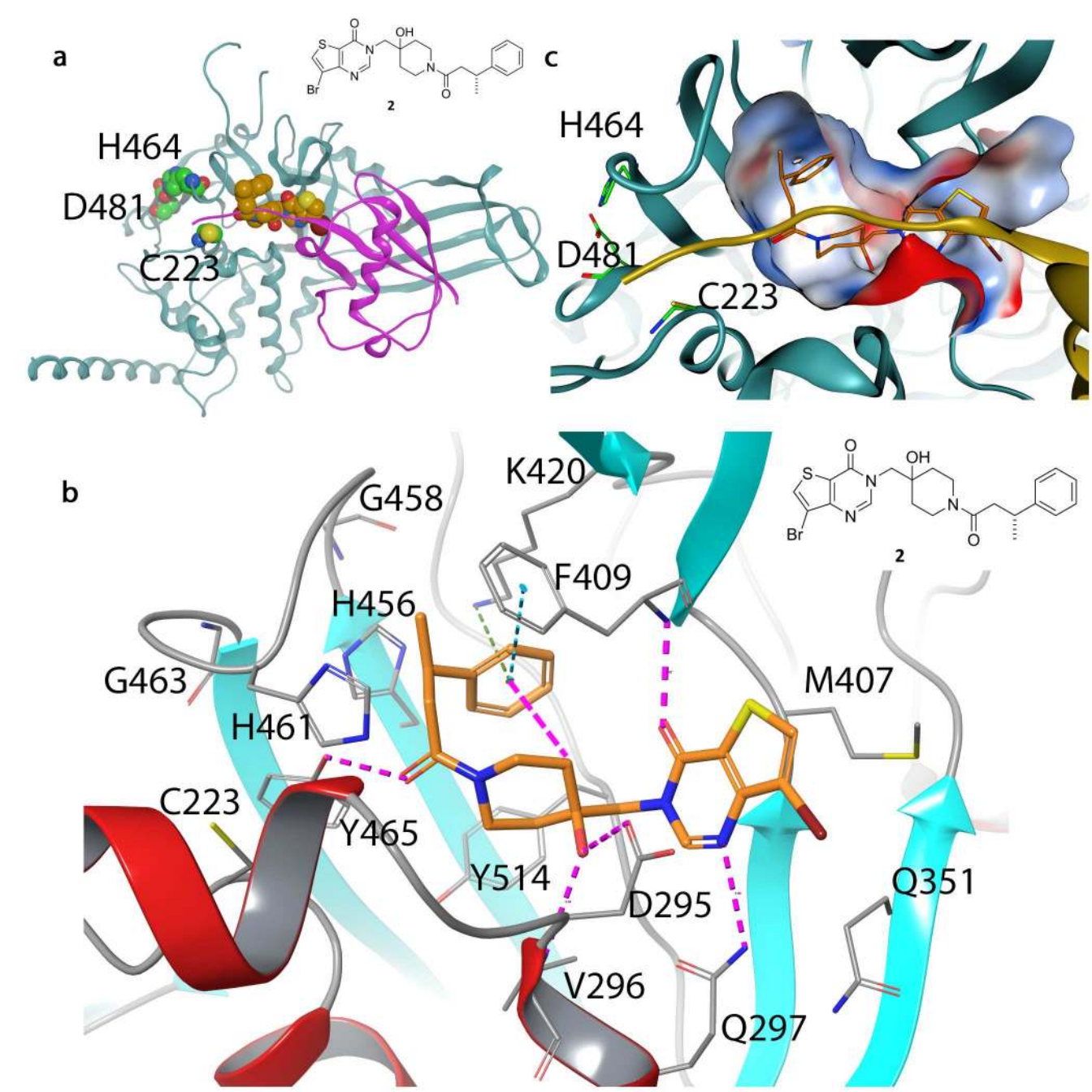
a
H464
D481
C223
2
c
H464
D481
C223
b
K420
G458
F409
H456
G463
H461
M407
C223
Y465
Y514
D295
Q351
V296
Q297
2

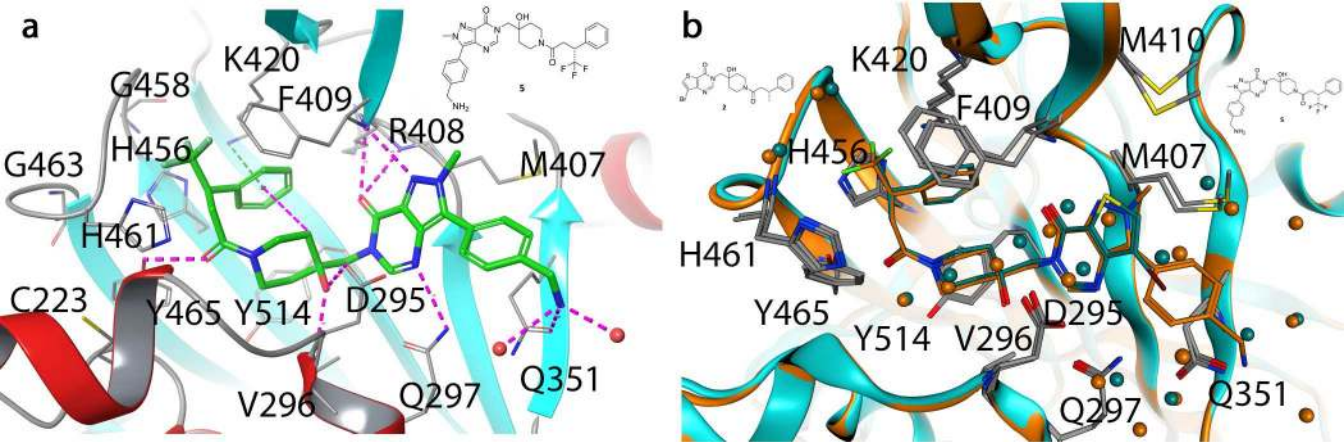
a
K420
G458
F409
R408
G463
H456
M407
H461
C223
Y465
Y514
D295
V296
Q297
Q351
b
K420
M410
F409
H456
M407
H461
Y465
Y514
V296
D295
Q297
Q351

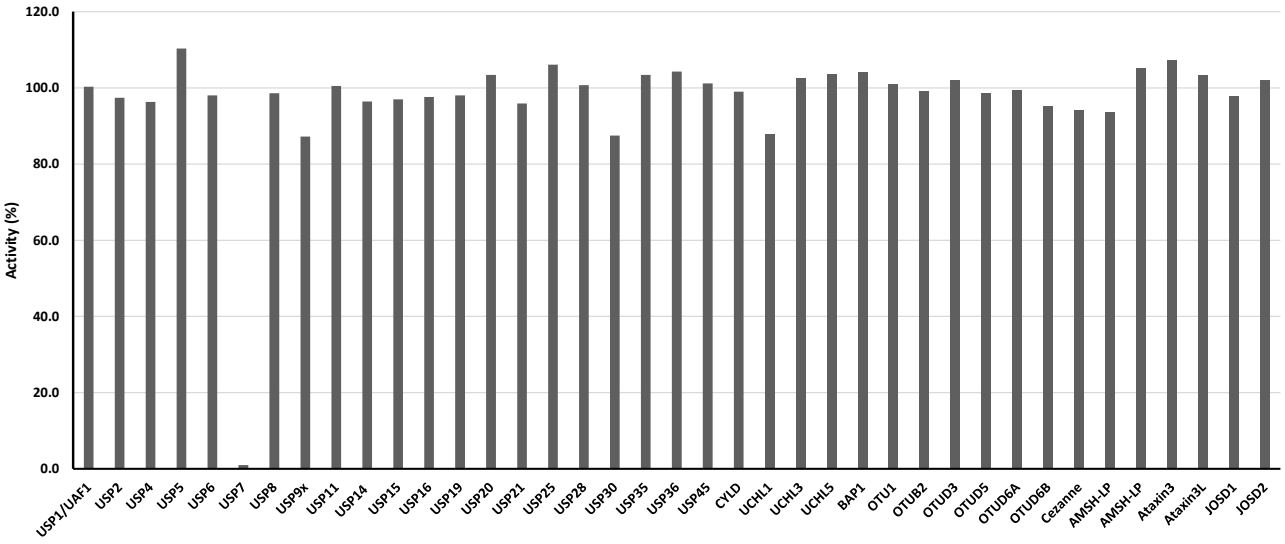
120.0
100.0
80.0
60.0
40.0
20.0
0.0
Activity (%)
USP1/UAF1
USP2
USP4
USP5
USP6
USP7
USP8
USP9x
USP11
USP14
USP15
USP16
USP19
USP20
USP21
USP25
USP28
USP30
USP35
USP36
USP45
CYLD
UCHL1
UCHL3
UCHL5
BAP1
OTU1
OTUB2
OTUD3
OTUD5
OTUD6A
OTUD6B
Cezanne
AMSH-LP
AMSH-LP
Ataxin3
Ataxin3L
JOSD1
JOSD2

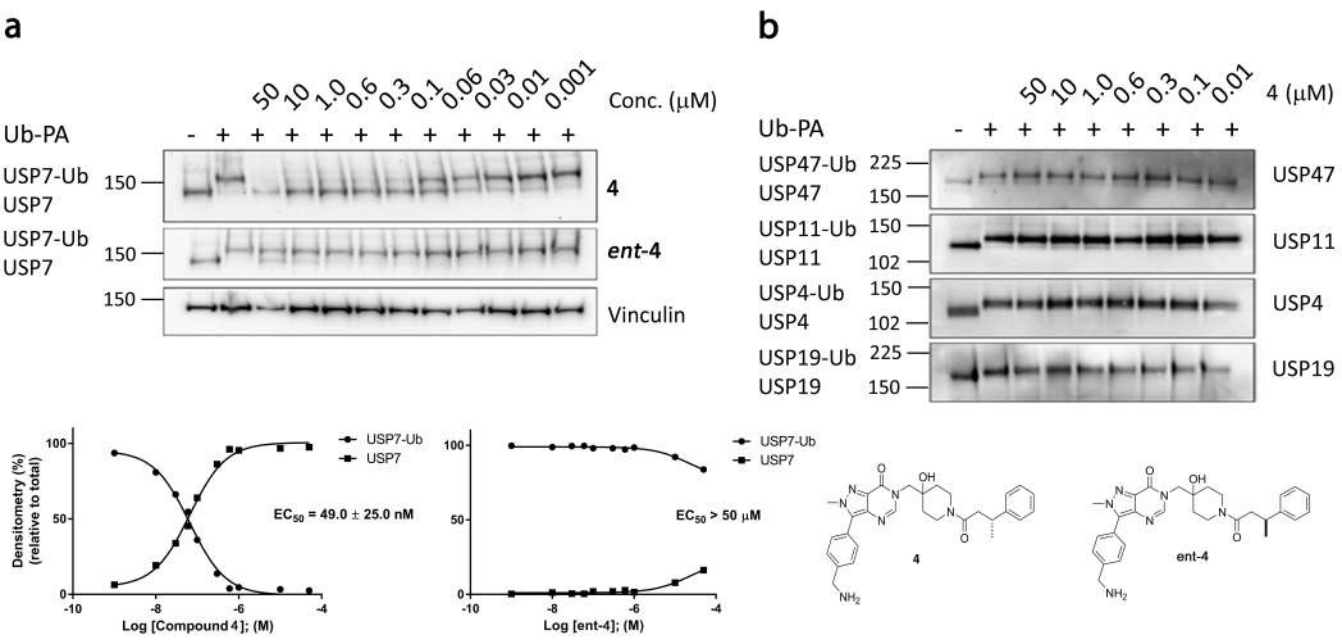
a
50 10 1.0 0.6 0.3 0.1 0.06 0.03 0.01 0.001
Conc. (μM)
Ub-PA
- + + + + + + + + + + +
USP7-Ub
USP7
150
4
ent-4
Vinculin
b
50 10 1.0 0.6 0.3 0.1 0.01
4 (μM)
USP47-Ub
USP47
225
150
USP11-Ub
USP11
102
USP4-Ub
USP4
USP19-Ub
USP19
Densitometry (%) (relative to total)
EC50 = 49.0 ± 25.0 nM
EC50 > 50 μM
Log [Compound 4]; (M)
Log [ent-4]; (M)
OH
NH2

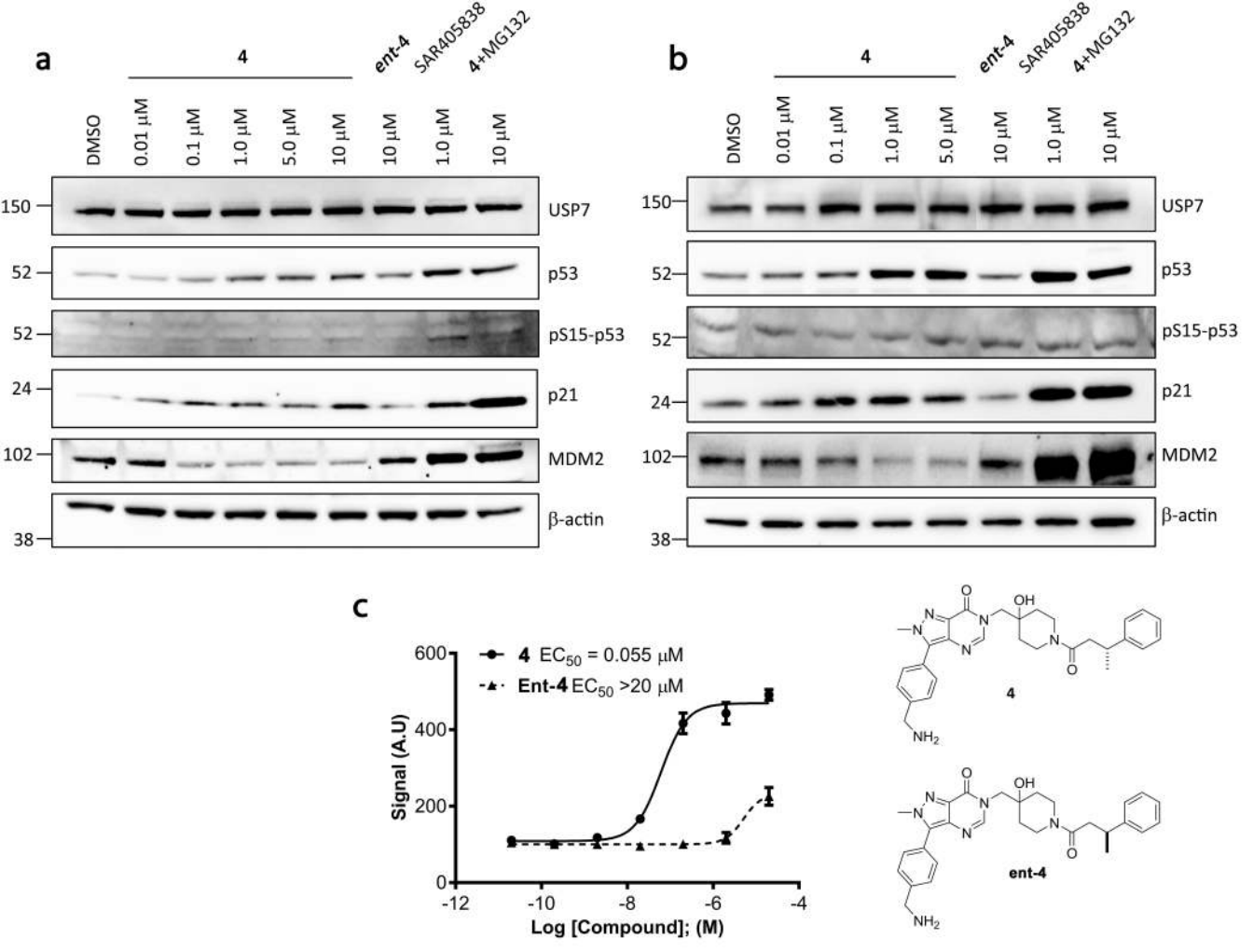
a
4
ent-4
SAR405838
4+MG132
DMSO
0.01 μM
0.1 μM
1.0 μM
5.0 μM
10 μM
10 μM
1.0 μM
10 μM
150
52
52
24
102
38
USP7
p53
pS15-p53
p21
MDM2
β-actin
b
4
ent-4
SAR405838
4+MG132
DMSO
0.01 μM
0.1 μM
1.0 μM
5.0 μM
10 μM
1.0 μM
10 μM
150
52
52
24
102
38
USP7
p53
pS15-p53
p21
MDM2
β-actin
c
4 EC50 = 0.055 μM
Ent-4 EC50 >20 μM
Signal (A.U)
600
400
200
0
-12
-10
-8
-6
-4
Log [Compound]; (M)
4
ent-4